1

Basics of Atomic Layer Deposition: Growth Characteristics and Conformality

Jolien Dendooven and Christophe Detavernier

Ghent University, Department of Solid-State Sciences, CoCooN Group, Krijgslaan 281, 9000 Ghent, Belgium

This chapter introduces some fundamentals and key advantages of the atomic layer deposition (ALD) technique. Following the standard example of a typical TMA/H_2O ALD cycle, the essential characteristics of true layer-by-layer growth (linearity, growth per cycle, saturation, and temperature window) are discussed. It is explained how the surface-controlled nature of the reactions ensures atomic-level thickness control and excellent conformality on 3D substrates, and the concept of plasma-enhanced ALD is introduced. In the second part of this chapter, the focus moves to *in situ* characterization methodologies that are often used in ALD research. The advantages of using *in situ* techniques to determine ALD growth characteristics are discussed, and examples of quartz crystal microbalance, quadrupole mass spectroscopy, spectroscopic ellipsometry, and optical emission spectroscopy (OES) are provided. In the third and final part, the conformality of ALD is reviewed. The use of macroscopic and microscopic lateral test structures for quantifying conformality will be addressed, as well as approaches to characterize conformal ALD in nanoporous materials.

1.1 Atomic Layer Deposition

1.1.1 Principle of ALD

ALD is a self-limited film growth method that is characterized by alternating exposure of the growing film to chemical precursors, resulting in the sequential deposition of (sub)monolayers [1, 2]. ALD was invented in the 1970s and further developed in the 1980s for the fabrication of luminescent ZnS and Al_2O_3 insulator films for electroluminescent flat-panel displays. It was only in the 1990s with the decreasing device dimensions and the resulting need for high-k oxides in microelectronics that the ALD technique has become a commercial success. Since then, a wide range of materials have been deposited by ALD including several oxides, nitrides, chalcogenides, and metals [3, 4]. As an example, we discuss the growth of an Al_2O_3 film using ALD. The basic process is illustrated in Figure 1.1. The initial situation is shown in Figure 1.1a, where a SiO_2 substrate,

Atomic Layer Deposition in Energy Conversion Applications, First Edition. Edited by Julien Bachmann.
© 2017 Wiley-VCH Verlag GmbH & Co. KGaA. Published 2017 by Wiley-VCH Verlag GmbH & Co. KGaA.

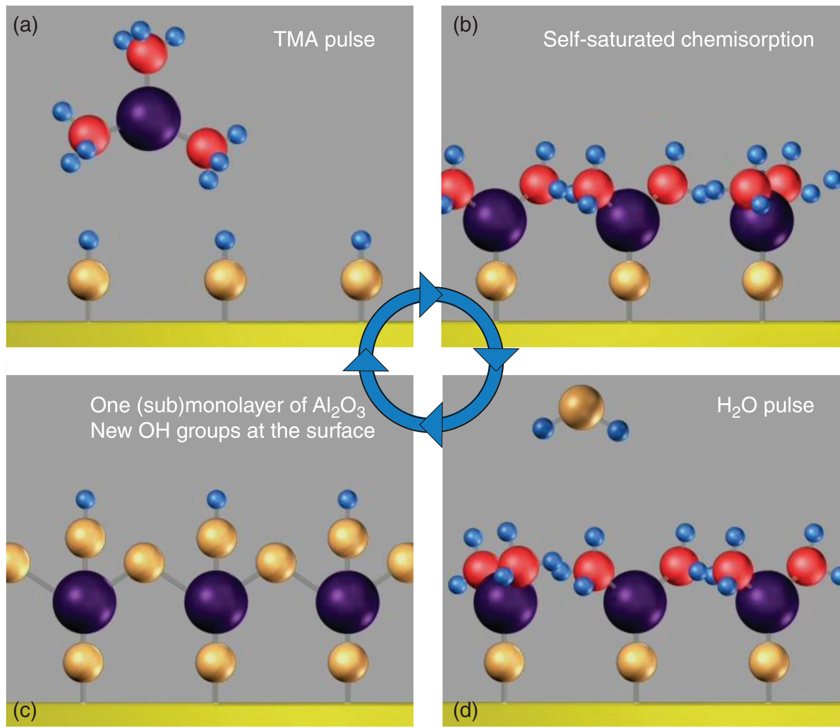

Figure 1.1 Principle of ALD, illustrated by the process for deposition of Al_2O_3 using TMA and H_2O. (Detavernier *et al*. 2011 [5]. Reproduced with permission of Royal Society of Chemistry.)

which is terminated by OH groups, is exposed to a pulse of trimethylaluminum vapor (TMA, typical exposure time of seconds). The TMA molecules adsorb on all exposed surfaces in the chamber and within pores, holes, and so on, in the sample. This deposition is self-limited, since the TMA molecules are chemisorbed through reaction with OH groups on the surface. Once all accessible OH groups have been consumed, no more TMA will adsorb (Figure 1.1b). The TMA pulse is followed by an evacuation of the reaction chamber through purging or pumping, where after a pulse of the reactant, for example, water vapor is introduced (Figure 1.1d). The water vapor reacts with the adsorbed TMA and hydrolyzes the residual methyl groups. This surface reaction results in the formation of a (sub)monolayer of alumina. In Figure 1.1c, one notices the presence of OH groups terminating the first alumina layer. Therefore, the ALD process can be repeated over and over again to deposit films, one (usually fractional) atomic layer at a time.

When compared to other film deposition techniques such as chemical vapor deposition (CVD), physical vapor deposition (PVD, i.e., evaporation or sputter deposition), or electrochemical deposition, ALD offers several advantages. The key advantage is the ability to deposit conformally into high aspect ratio (AR) structures. Other advantages include (i) control of the layer thickness at the Angstrom level (the limited deposition rate that is regarded as a disadvantage of ALD is nowadays considered a unique advantage because it allows for the

deposition of ultrathin films (e.g., <10 nm)); (ii) chemical selectivity, enabling area-selective ALD where deposition only occurs in those regions of the surface where reactive surface sites are present [6–13]; and (iii) industrial scalability. Indeed, because ALD is based on the exposure of a surface to a precursor vapor and, therefore, is nondirectional, one can design batch reactors, where many substrates can be coated simultaneously [14, 15]. In addition, large area processing based on spatially separated reagent flows is being actively explored today, especially for photovoltaic and flexible electronic applications [16].

Over the past decades, hundreds of ALD chemistries have been found for depositing a variety of materials. A review paper by Puruunen [3] from 2005 and the more recent update by Miikkulainen *et al*. [4] provide an excellent review of the available process chemistries for deposition of oxides, nitrides, chalcogenides, and metals using ALD (Figure 1.2).

ALD currently is mainly used in the microelectronics industry, for example, for growing high-*k* gate oxides. Its ability for conformal deposition into high AR features offers the potential for breakthroughs in fields where ultrathin coatings are required on nanostructured, nanoporous, or fibrous substrates. Since the early 2000s, researchers have been exploring ALD as a generic coating technique for a variety of nanostructures, as illustrated in a number of review papers [5, 17–21]. ALD deposition has, for example, been reported for coating anodic alumina [22–24], aerogel [25–28], nano-sized powder [29–34], nanowires [35–38], and fibrous materials [39–42]. Potential application fields include catalysis, gas separation, sensors, batteries, capacitors, fuel cells, photovoltaics, and photonics.

1.1.2 ALD Growth Characteristics – Linearity, Saturation, and ALD Window

The ideal ALD process is characterized by a linear increase of the amount of deposited material as a function of the number of ALD cycles. One usually defines the "growth per cycle" or GPC as the amount of material deposited (or the equivalent thickness increase) per ALD cycle. While GPC is a practical concept that is often used in everyday communication in the laboratory as well as in the literature, it is important to realize that the "apparent" GPC value does not reflect in any way the chemical reaction kinetics during the deposition process but is determined by the number of chemisorption sites on the growth surface, which will depend on the reactivity and number of accessible surface sites and even on surface morphology. As illustrated in Figure 1.3, one often observes that the apparent GPC is substrate dependent at the start of the ALD process and that it takes a certain number of cycles before a steady-state GPC value is obtained. This is caused by the fact that the chemical sites on the original substrate can have a different reactivity compared to the chemical sites on the surface of the as-grown material. While substrate inhibition and the resulting delay in film nucleation/growth may be considered a disadvantage at first sight, this effect can in fact be very beneficial when one is targeting area selective ALD. The data for Pt ALD shown in Figure 1.3 illustrates that the "apparent" GPC can strongly depend on the surface morphology. Indeed, ALD growth on a rough surface will have an apparently higher GPC, as more material can be deposited per cycle in view of the larger effective surface area that is available for growth.

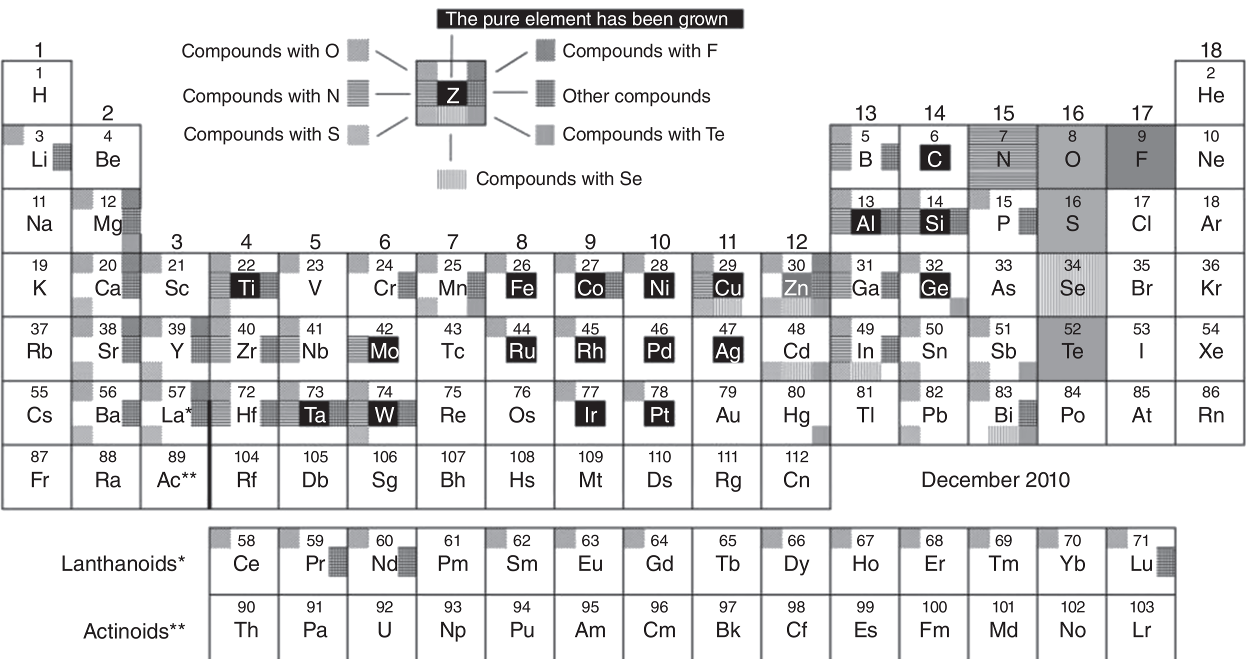

Figure 1.2 Overview of materials grown by ALD. Growth of pure elements as well as compounds with oxygen, nitrogen, sulfur, selenium, tellurium, fluorine, and other compounds grouped together is indicated through shadings of different types at different positions. (Miikkulainen *et al*. 2013 [4]. American Institute of Physics.)

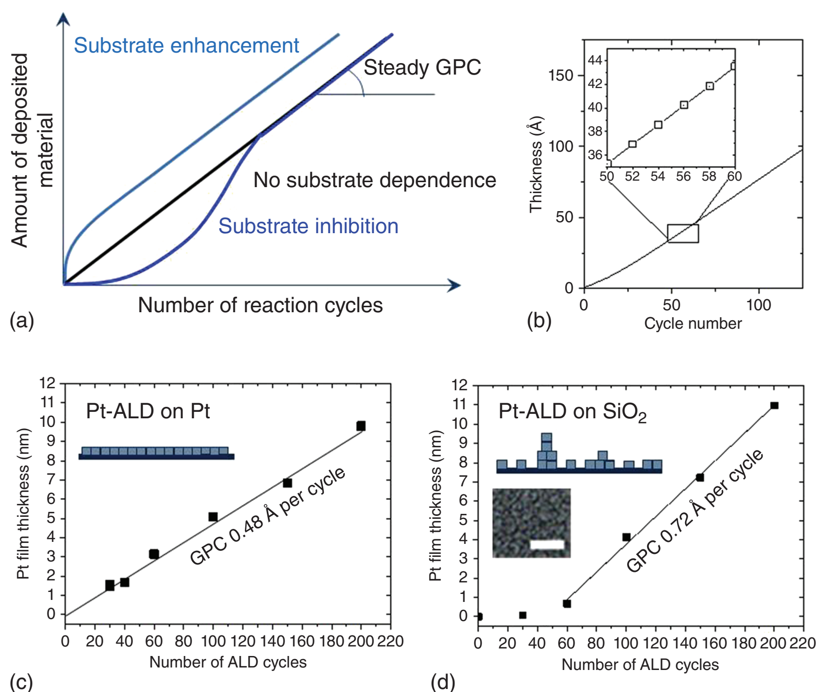

Figure 1.3 Linear increase of the amount of deposited material as a function of the number of ALD cycles: principle (a: [43]), *in situ* ellipsometry data for Al_2O_3 ALD (b), and film thickness data for a $MeCpPtMe_3/O_3$ process at 150 °C with 2D growth (on a sputtered Pt surface (c)) versus island-type growth on a SiO_2 surface (d) [44], illustrating that GPC values should be interpreted as "apparent" values that depend on the surface conditions (the scale bar on the electron microscopy image is 100 nm). (Reproduced with kind permission of Annelies Delabie.)

The self-saturating nature of the surface reactions occurring during both half cycles can be considered as the defining characteristic of ALD. When developing novel ALD processes, demonstrating "saturation" is a key goal. Saturation curves are typically achieved by running several deposition experiments at the same substrate temperature, while varying the exposure dose during one of the half cycles. The GPC is then plotted as a function of the exposure dose (most often as a function of exposure time), as illustrated in Figure 1.4 for the TMA/H_2O process.

Finally, the "ALD window" is defined as the temperature range in which saturated growth conditions prevail (Fig. 1.5a). When the temperature is too low, one often observes that growth is no longer possible, because the thermal energy is insufficient to drive the surface chemistry. In some cases, an apparently faster growth is observed, which is often related to the occurrence of physisorption instead of the self-saturating chemisorption that is desirable. At high temperatures, higher growth rates are often observed, which are caused by thermal decomposition of the precursor on the hot surface (essentially resulting in CVD-type growth). In some cases, the growth rate is observed to decrease at high temperature because of thermal desorption of chemisorbed species that

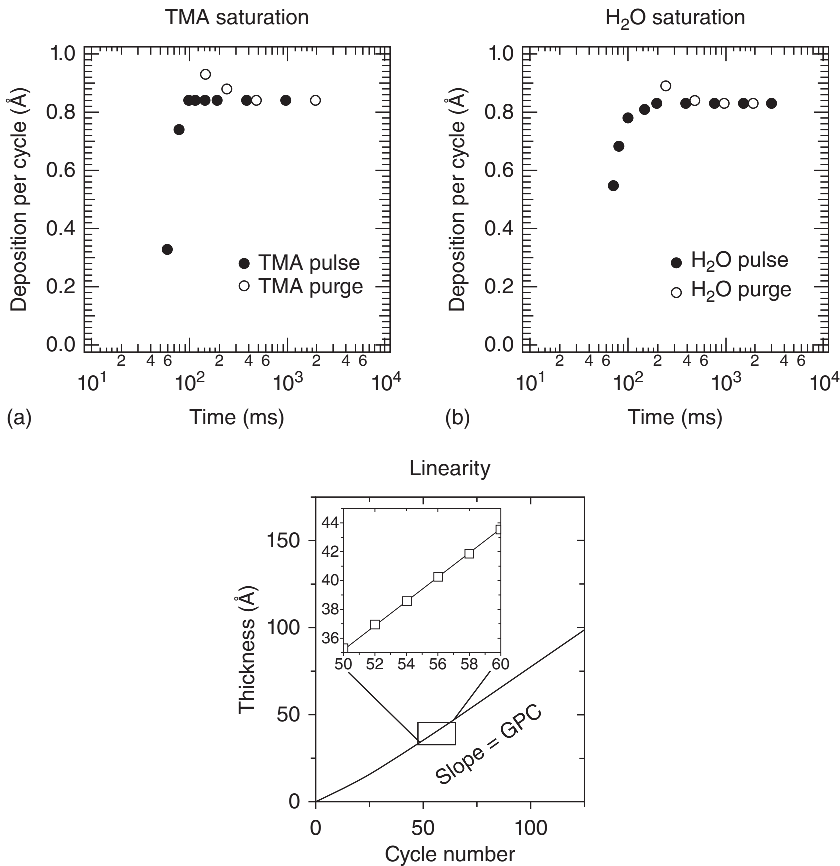

Figure 1.4 Saturation during the TMA and H_2O exposures for ALD of Al_2O_3. (Puurunen 2005 [3]. Reproduced with permission of American Institute of Physics.)

are required for growth. It is important to note that the GPC is not necessarily constant within the ALD window. Indeed, even for the TMA/H_2O process, which exhibits saturated growth from 180 to 380 °C [45], the GPC decreases for increasing temperature, as illustrated in Figure 1.5b. Although self-saturating chemisorption is achieved across the entire ALD window, the GPC decreases because of dehydroxylation of the growth surface at higher temperatures.

1.1.3 Plasma-Enhanced ALD

In ALD processes such as the described TMA/H_2O process, the activation energy required for the surface reactions is solely provided by heating the sample. Therefore, these processes are called thermal ALD processes. Alternatively, the reactant can be preactivated by means of a plasma source (plasma-enhanced ALD or PE-ALD) [46]. A plasma is a gaseous mixture of neutral and charged particles that is macroscopically neutral. Most materials processing plasmas are generated

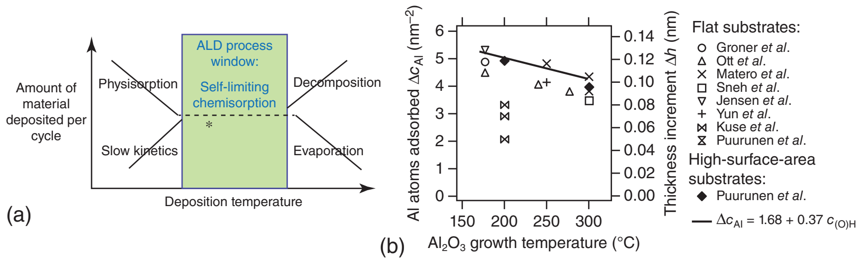

Figure 1.5 Effect of substrate temperature on ALD: (a) schematic [43] and (b) a compilation of data for the TMA/H_2O process by Puruunen [3], illustrating that the GPC may vary as a function of temperature within the "ALD window." (Puurunen 2005 [3]. Reproduced with permission of American Institute of Physics.)

by a strong electric field at low gas pressures (<10 Torr). Any electrons present in the gas are accelerated to high kinetic energies. When these electrons collide with the atoms and/or molecules of the background gas, they are able to ionize, excite, or dissociate these gas species, thus yielding electrons, ions, reactive atomic and/or molecular neutrals (radicals), and photons. The created ions and electrons are in turn accelerated by the applied field. Because of the large difference in mass, the electrons will gain more kinetic energy compared to the ions, thus leading to "hot" electrons with an average temperature of several 10^4 K (several electron volts), while the other gas species remain approximately at reactor temperature (300–500 K). Consequently, low-pressure plasmas are not in thermal equilibrium. The degree of ionization, that is, the fraction of ionized particles in the plasma, is typically in the range 10^{-6} to 10^{-3}.

1.1.3.1 Plasma Configurations for Plasma-Enhanced ALD

Plasma-enhanced ALD (PE-ALD) uses the species generated in a plasma as reactants. Mainly O_2, N_2, NH_3, and H_2 plasmas (or mixtures thereof) have been used for the growth of oxides, nitrides, and metal films [46]. As mentioned before, plasmas produce energetic ions and reactive radicals, for example, O_2 can dissociate in two O radicals. Because the degree of ionization is rather low in typical PE-ALD plasmas, the radicals are expected to play the key role in the surface reactions. Nevertheless, ions that arrive at the sample surface can provide additional energy to the surface, leading to physical changes in the sample, such as smoothening or densification. However, they can also be implanted in the growing film or substrate, which is often unwanted or induce defect creation. Because radicals have a longer lifetime compared to charged particles, they are less confined to the plasma discharge region. Therefore, the level of ion bombardment can be controlled by the plasma configuration.

The different types of plasma configurations used for PE-ALD are schematically depicted in Figure 1.6. In the first configuration, the plasma is formed in a cavity, which is separated from the deposition chamber. The ions and electrons recombine during transport to the ALD reaction zone, and only the longer lived radicals can reach the substrate. Therefore, this configuration is called "radical-enhanced"

or “radical-assisted” ALD. Its main advantage is that ion-induced damage of the film or substrate is completely avoided. However, also the flux of reactive radicals will be reduced compared to plasma configurations where the plasma is in contact with the sample. This is clearly the case in a “direct plasma” configuration. Here, a capacitively coupled radio-frequency (RF) generator powers one electrode, while the substrate is placed on the second, generally grounded, electrode. The sample is in close contact with the plasma and is thus exposed to high fluxes of radicals and ions. Consequently, uniform coatings can be achieved with short plasma exposures, but, depending on the processing conditions, severe ion bombardment can be an issue. In the “remote plasma” configuration, the plasma source is placed upstream of the substrate. Very often, an inductively coupled plasma is generated in a glass or quartz tube surrounded by a radio-frequency (RF) coil. For a remote O_2 plasma, ion fluxes in the range 10^{12}–10^{14}/cm^{2}s have been measured at the sample stage, with ion energies below 35 eV. These values are considered low enough to not create substantial film or substrate damage. On the other hand, however, it was shown that the UV photons (9.5 eV) created in the plasma can induce electrical defects [47]. The fourth plasma configuration can be considered as a direct plasma operating in a remote configuration by placing a grid in between the top electrode and the sample [48]. Because this grid acts as the bottom electrode, the sample stage is no longer involved in the plasma generation. As such, significant ion bombardment of the substrate is avoided.

1.1.3.2 Reactions in Plasma-Enhanced ALD

Most reaction mechanism studies of PE-ALD in the literature concern O_2 plasma-based processes, mostly resulting in the growth of oxides [49]. Heil *et al.* studied the reaction products formed during the Al_2O_3 process from trimethylaluminum (TMA) and O_2 plasma by means of *in situ* mass spectroscopy and OES [50]. These measurements revealed the formation of CO, CO_2, and H_2O during the plasma step, which was attributed to the combustion of the methyl ligands (of the adsorbed TMA molecules) on the surface by the O radicals. Using *in situ* infrared spectroscopy, Rai *et al.* showed that these combustion-like reactions produce OH groups and carbonates on the surface during the O_2 plasma step in the PE-ALD of Al_2O_3 [51] and TiO_2 [52]. They furthermore demonstrated that a prolonged exposure of the carbonates to the O_2 plasma decomposes them in CO_2 and CO, meaning that the OH groups are the dominant chemisorption sites in the subsequent precursor step, as in thermal ALD. Pure metallic films are often grown with H_2 plasma as the reducing reactant. Kim *et al.* studied the reaction mechanism underlying the PE-ALD of Ti using $TiCl_4$ and H_2 plasma. They proposed that the reaction proceeds via an Eley–Rideal mechanism: the H radicals react with the adsorbed Cl species from the gas phase to form HCl that then is desorbed from the surface [53].

1.1.3.3 Advantages and Challenges of Plasma-Enhanced ALD

Key advantages of PE-ALD include a higher film density, lower impurity content, better stoichiometry, and improved electronic properties. From a process perspective, the use of radicals enables deposition at lower substrate temperatures, which can be a key advantage when coating polymers. Moreover, PE-ALD

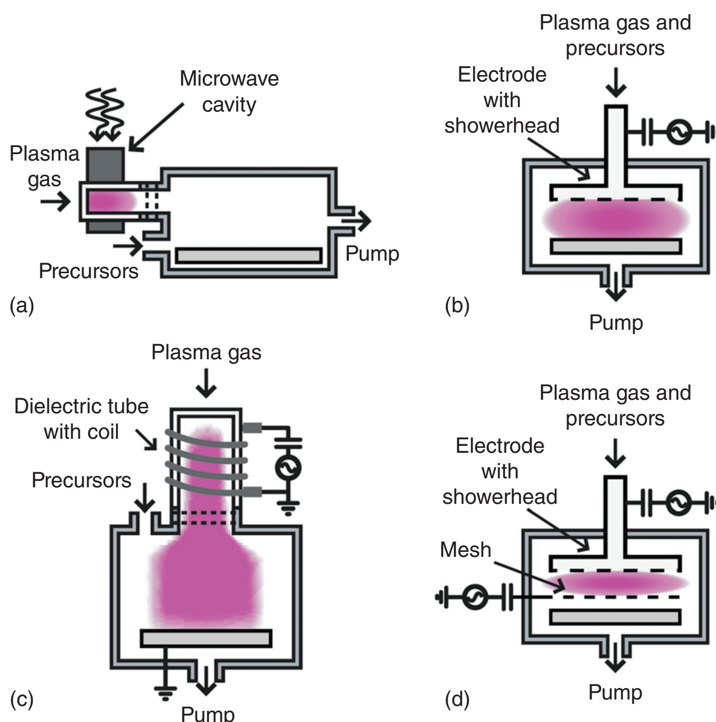

Figure 1.6 Plasma configurations used for PE-ALD. (a) Radical-enhanced ALD. (b) Direct plasma. (c) Remote plasma. (d) Direct plasma in remote configuration. (Profijt *et al*. 2011 [46]. Reproduced with permission of American Institute of Physics.)

typically enables a slightly higher growth rate, shortening the overall deposition time. More importantly, the use of radicals from a plasma increases the choice of precursors for deposition of a specific coating, for example, the beta-diketonate precursors show low reactivity to water vapor but react readily with oxygen radicals. Some of these benefits of PE-ALD are illustrated in Figure 1.7.

There are, unfortunately, also specific disadvantages to using plasma during an ALD process. Firstly, recombination of the radicals on the sidewalls limits the conformality in high AR structures. Secondly, the ions and UV photons from the plasma may generate specific defects in the growing layer. Thirdly, from a process point of view, the use of a plasma requires more complicated and therefore expensive reactor designs.

1.2 *In Situ* Characterization for Studying ALD Processes

When exploring ALD processes, *in situ* characterization techniques offer the advantage that the ALD process no longer occurs in a "black box" but that the surface chemistry and the properties of the growing film can be monitored in real time. Since ALD is, in essence, surface chemistry, one would ideally like to use, for example, the electron- and ion-spectroscopy techniques that have been

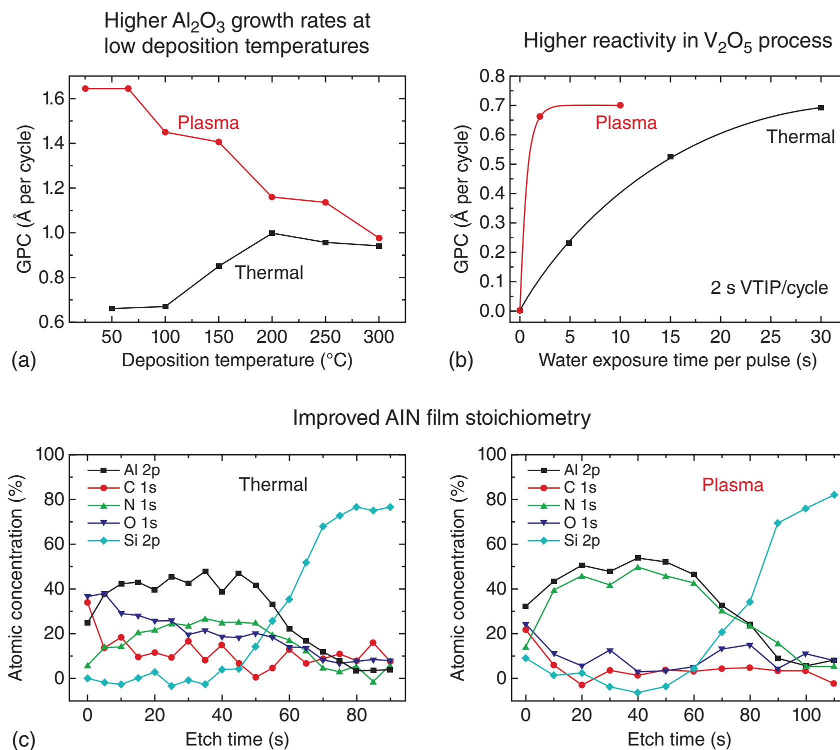

Figure 1.7 Illustration of some of the advantages of (remote) PE-ALD as compared to thermal ALD. (a) Growth per cycle (GPC) as a function of deposition temperature for the growth of Al_2O_3 using 2 s TMA and 5 s H_2O or H_2O plasma. (b) GPC of V_2O_5 as a function of H_2O exposure time for thermal and PE-ALD using vanadyl triisopropoxide (VTIP) as V precursor (data taken from [54]). (c) X-ray photoelectron spectroscopy profiles for AlN films grown by thermal and PE-ALD using 2 s TMA and 5 s NH_3 or NH_3 plasma at 250 °C. The plasma power was in all cases 300 W.

developed by surface scientists. Unfortunately, it is very difficult to implement these techniques truly "*in situ*" on an ALD reactor, since the ultrahigh vacuum that is typically required by these techniques is not compatible with ALD process conditions.[1] Over the past decade, a variety of *in situ* techniques have been developed, and several have become available on commercial ALD reactors.

1.2.1 Quartz Crystal Microbalance

Quartz crystal microbalance (QCM) is a well-known technique to monitor thin-film deposition [55, 56]. As material is deposited onto an oscillating

1 X-ray photoelectron spectroscopy, low-energy ion spectroscopy, and scanning tunneling microscopy have been implemented as "*in vacuo*" techniques, where ALD is performed in a dedicated reactor and the sample is moved from the ALD reactor under vacuum conditions (i.e., without exposure to ambient air) into a ultrahigh vacuum (UHV) chamber for characterization. Evidently, this can provide a wealth of useful data on the surface reactions during ALD. However, because of the need for moving the sample, these techniques are not discussed here, as we have limited the discussion to true "*in situ*" techniques.

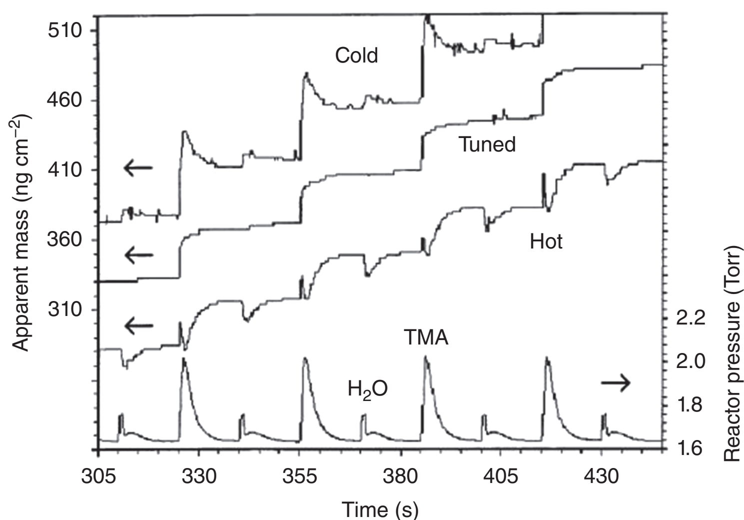

Figure 1.8 QCM measurement during TMA/H_2O ALD, illustrating the impact of temperature effects on the data. Only the "TUNED" data reflects the actual deposition onto the crystal. For the "COLD" and "HOT" traces, apparent mass changes were recorded due to temperature fluctuations during gas pulsing. (Rocklein and George 2003 [58]. Reproduced with permission of American Chemical Society.)

piezoelectric crystal, the resonant frequency of the crystal decreases. By measuring this shift in resonant frequency, the added mass can be determined with a resolution below 1 ng cm^{-2}. The key challenge to implement QCM during ALD concerns (i) preventing backside deposition [57] and (ii) dealing with temperature effects [58]. Indeed, the resonant frequency is also strongly dependent on the temperature of the QCM crystal. For AT-cut quartz crystals, the specified temperature range is −45 to 90 °C. At higher temperatures, small temperature changes can lead to significant changes in resonant frequency, and hence in apparent mass changes, even when pulsing inert probe gases onto the crystal. Lower temperatures prior to the QCM lead to positive mass transients. More elevated temperatures prior to the QCM lead to negative mass transients. Unreactive probe gases can be employed to optimize the temperature profile to minimize the temperature-induced apparent mass changes. QCM can be a simple and powerful technique, provided that sufficient care is taken during the measurement and analysis, as apparent mass transients and apparent mass drifting can lead to misinterpretation of ALD surface chemistry and produce error in measured ALD growth rates, as illustrated in Figure 1.8.

1.2.2 Quadrupole Mass Spectrometry (QMS)

QMS can be used during ALD to identify and monitor the gaseous species that are present in the reactor and/or the exhaust line [59, 60]. Commercial systems provide an inlet orifice for gas sampling. Electron impact from a filament then results in ionization and molecular fragmentation of the gas molecules. The ionized species are then sent through a quadrupole filter, which transmits a specific

mass/charge ratio. As the quadrupole is scanned, for example, a Faraday cup is used to measure the ion current.

Ritala *et al*. reported a dedicated system with a sample point near the hot zone of the ALD reactor to avoid precursor condensation [61, 62]. While this can be beneficial for easily condensable vapors, many gases can also be detected using a standard commercial QMS, for example, attached to the exhaust line of the reactor [63]. To enhance the QMS signal, a very useful trick can be to increase the total surface area in the ALD reactor. As $\sim 10^{14}$ reaction products will be released per square centimeter of sample during ALD, increasing the surface area of the sample (e.g., by including a large number of glass slides or powder particles in the reactor) will increase the amount of gaseous reaction products, facilitating detection.

1.2.3 Spectroscopic Ellipsometry

Spectroscopic ellipsometry (SE) is a powerful optical technique for the determination of the optical constants and thickness of thin (multi)layers deposited on a substrate. SE does not directly measure these film properties; instead, it measures the change in polarization of a light beam upon reflection from the sample. Therefore, from an instrumentation point of view, ellipsometry requires (i) a light source and a polarizer to define the polarization of the incoming beam and (ii) a polarization analyzer and a detector unit to determine the polarization of the reflected light.

An ellipsometric measurement is commonly described in terms of Ψ and Δ with

$$\tan(\Psi)\exp(i\Delta) = R_p/R_s$$

where R_p and R_s are the complex Fresnel coefficients of the sample for p- (in the plane of incidence) and s- (perpendicular to the plane of incidence) polarized light, respectively (see Figure 1.9). In SE, the Ψ and Δ parameters are measured for a range of photon wavelengths. In order to relate the SE data to the actual properties of the sample, a model of the sample must be constructed from which the modeled ellipsometric parameters Ψ_{mod} and Δ_{mod} can be calculated using the Fresnel equations. In general, a multilayer model is built, where each layer is characterized by a thickness and a certain dispersion relationship of the optical

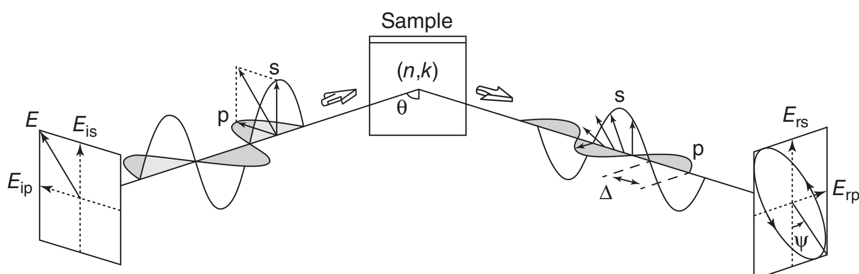

Figure 1.9 Schematic representation of a basic ellipsometer system. (Fujiware 2007 [64]. Reproduced with permission of John Wiley and Sons.)

constants. Finally, the adjustable model parameters are varied to find the best fit of the calculated Ψ_{mod} and Δ_{mod} values to the measured SE data [65]. The data in Figure 1.3b illustrates the Angstrom-level thickness sensitivity of the SE technique during ALD of Al_2O_3.

1.2.4 Fourier Transform Infrared Spectroscopy

Fourier transform infrared spectroscopy (FTIR) detects vibration modes of molecular bonds in the sample [66]. The key challenge in using FTIR during ALD concerns the fact that one is trying to measure the IR absorption caused by a (sub)monolayer on the surface of the sample. This requires an excellent signal/noise ratio and a very "clean" measurement, as traces of gaseous H_2O and CO_2 along the beam path may create spurious signals in the measurement [67]. Several dedicated setups have been designed for IR surface spectroscopy, including transmission geometries through a double polished Si wafer [68], transmission geometries using ZrO_2 powder pressed into metal grid to enlarge the effective surface area and hence enhance the signal [69], attenuated total reflection measurements [70], and, more recently, also IR reflection absorption spectroscopy [71]. Figure 1.10 shows typical *in situ* FTIR difference spectra before/after specific steps during a TMA/H_2O ALD process.

1.2.5 Optical Emission Spectroscopy

Optical emission spectroscopy (OES) can be used to measure the intensity of light emitted by a plasma as a function of wavelength and, as such, is a very convenient technique for *in situ* monitoring of PE-ALD processes. The spectral lines in

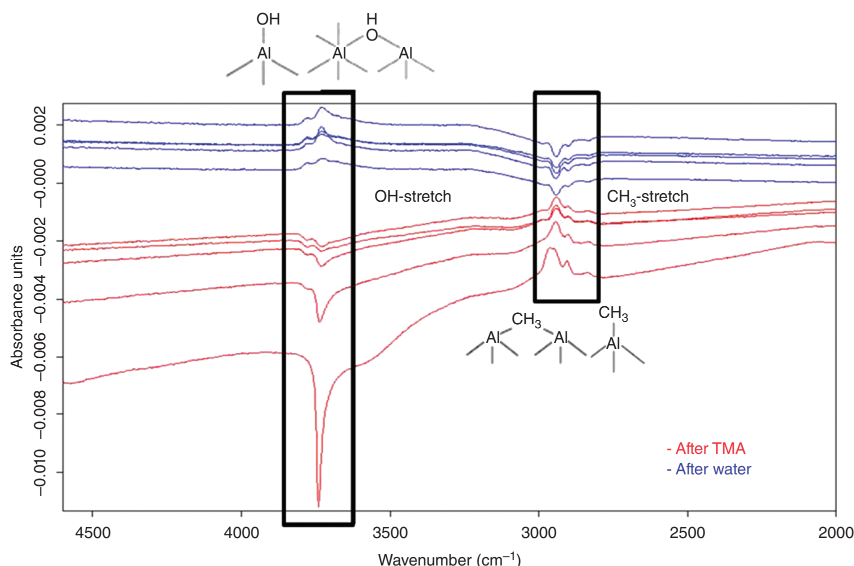

Figure 1.10 Difference FTIR spectra acquired during the initial cycles of a TMA/H_2O ALD process.

the emission spectrum originate from the radiative decay of electronically excited states of the plasma species. Therefore, OES spectra can reveal information on the presence of particular excited ions, atoms, and molecules in the plasma, and, because these species can be both reactant and reaction products, also about the reactions that take place in the gas phase, at the chamber walls, or at the surface of the growing ALD film [72].

1.2.6 Other *In Situ* Techniques

Other *in situ* techniques that have been implemented on ALD reactors include reflection high-energy electron diffraction [73], a thermopile for measuring reaction enthalpy [74], sheet resistance measurements for monitoring coalescence of metal layers [75], gravimetry [76], optical reflectometry [77], gas conductance measurements [78] for monitoring pore size reduction, and *in situ* ellipsometric porosimetry (EP) [79] for monitoring ALD in nanopores.

Optical techniques have proven to be the easiest to use in practice, since no measuring equipment needs to be incorporated within the ALD reactor. They can remotely probe the sample surface and only require entry and exit windows to pass light into and out of the reactor. Recently, several groups have explored expanding the spectral range from UV/Vis (used for SE, with quartz windows) and IR (used for FTIR, with KBr windows) toward X-rays (with Be windows), thus opening up an even wider variety of characterization possibilities [80]. Although standard X-ray-based analysis techniques such as X-ray reflectivity and diffraction using lab-based X-ray sources have proven valuable for *ex situ* characterization of ALD deposited thin films, most *in situ* experiments during ALD require synchrotron-based X-rays. To enable *in situ* studies during ALD, it is important to limit the impact of the prolonged purge or evacuation times that are introduced between subsequent ALD (half)cycles to perform the measurements. The high photon flux at a synchrotron facility is beneficial in this respect, because it allows for shorter acquisition times compared to lab-based X-ray sources. The high intensity X-ray flux also lowers the detection limit, enabling the study of layer growth from the very first ALD cycle onward. A second main advantage of synchrotron sources is their unique ability to tune the photon energy to a specific experiment and material system. In recent years, the use of synchrotron-based X-rays has broadened the available tool box of *in situ* methods to X-ray fluorescence (XRF, measuring film composition) [81, 82], X-ray absorption spectroscopy (XAS/EXAFS, measuring the local atomic environment) [83, 84], X-ray photoelectron spectroscopy (XPS, measuring surface composition and oxidation state), X-ray diffraction (XRD, measuring film crystallinity, grain size), X-ray reflectivity (XRR, measuring film thickness, roughness, and density), and grazing-incidence small-angle X-ray scattering (GISAXS, measuring surface morphology) [85, 86].

1.3 Conformality of ALD Processes

The deposition of uniform coatings into deep structures such as holes, trenches, and (nano)pores is becoming increasingly important in the rapidly growing

field of nanotechnology. Among all the thin-film growth techniques, ALD can achieve the highest conformality, that is, the most uniform thickness over micro- and nanoscale 3D features. The excellent conformality of ALD is a direct consequence of the self-saturated surface reaction control, as opposed to flux-controlled deposition in, for example, PVD and CVD. In CVD, the growing film is usually exposed to simultaneous flows of precursor vapor and reactant gas (instead of the sequential pulses in ALD), and the growth rate of the film generally depends on the local gas flux. During coating of deep features in which the gas transport is diffusion-limited, the surface region near the entrance of these features will receive reactant fluxes that can be several orders of magnitude larger than the fluxes arriving at the surfaces deeper in the structures. Therefore, deposition techniques where the growth rate is flux-controlled are less convenient for coating high AR structures or porous materials, because the entrance region of features such as holes, trenches, and pores tends to get clogged during the early stages of deposition. In addition, in ALD, the regions near the entrance of the holes, trenches, or pores in a material will experience a larger flux of precursor vapor and, therefore, will become saturated much sooner than the interior surfaces. Once saturated, however, no further reaction will occur near the openings, and one can "simply" expose the entire sample for a sufficient amount of time until the precursor molecules have diffused into the deep features and have saturated the available chemisorption sites throughout the interior surface of the material.

ALD has proven to be an effective technique for the deposition of conformal coatings in features with a high AR [87–89]. Nevertheless, achieving a good conformality along the entire depth of high AR structures requires careful optimization of the ALD process parameters.

1.3.1 Quantifying the Conformality of ALD Processes

The most common way to demonstrate the conformality of an ALD process is by deposition into deep microscopic trenches (typical width $<1\ \mu m$) and subsequent characterization by cross-sectional scanning electron microscopy (SEM) or transmission electron microscopy (TEM), as illustrated in Figure 1.11. This method yields a stop/go-type result in the sense that it provides a means to verify whether full coverage could be achieved or not. Obtaining a quantitative film thickness profile along the length of the trench is, however, difficult.

Several groups successfully obtained thickness profiles for ALD films deposited in anodic aluminum oxide (AAO) [23, 91]. AAO can be prepared by a two-step electrochemical anodization of aluminum films [92–94]. It consists of well-defined parallel cylindrical pores (typical diameters 30–500 nm) and is therefore an attractive material for model studies of ALD in high AR nanostructures. After ZnO ALD in an AAO membrane, Elam *et al*. obtained Zn coverage profiles as a function of depth in the membrane using electron probe microanalysis (EPMA) line scans along the axis of the pores [22]. Figure 1.12 shows the diffusion-limited behavior of ZnO ALD in AAO nanopores with a diameter of 65 nm. Indeed, increasing the Zn-precursor exposure time allowed for a deeper penetration and deposition of the precursor molecules in the hole.

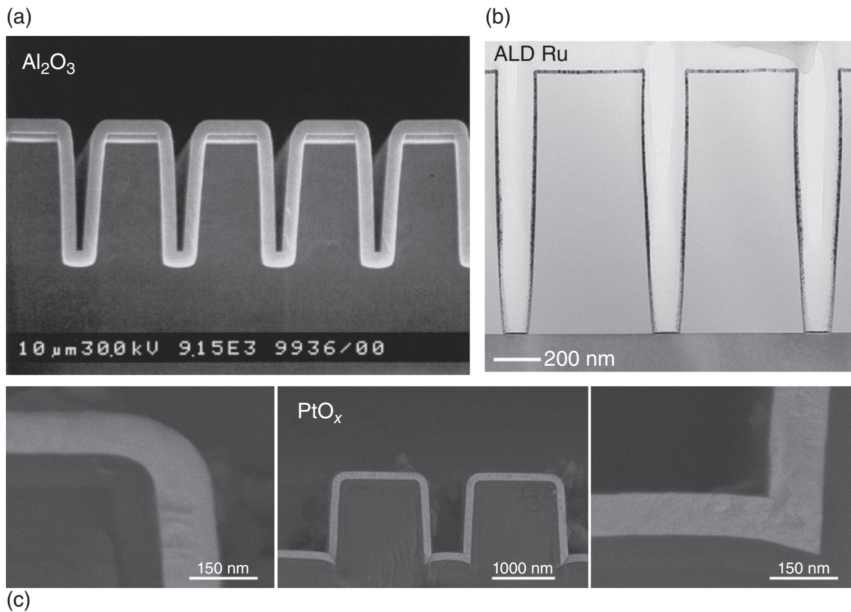

Figure 1.11 (a) Cross-sectional SEM image of a 300 nm-thick Al_2O_3 film deposited on a Si wafer with trench structures (Ritala *et al*. 1999 [89]. Reproduced with permission of Wiley.). (b) Cross-sectional TEM of a conformal Ru ALD coating on a trench-patterned substrate (Kim *et al*. 2009 [18]. Reproduced with permission of Wiley.). (c) Cross-sectional Field Emission Scanning Electron Microscopy (FESEM) images of a conformal PtO_x film deposited on a Si substrate with trench structures. (Hämäläinen *et al*. 2008 [90]. Reproduced with permission for Elsevier.)

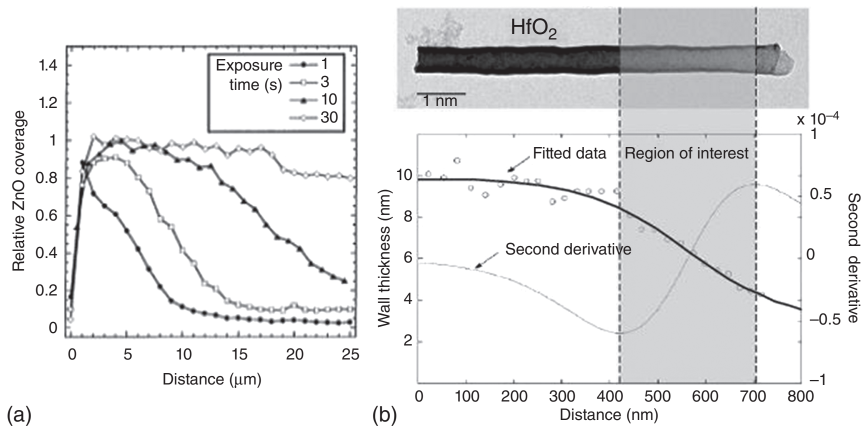

Figure 1.12 Film thickness/coverage profiles obtained for ALD in AAO nanopores. (a) Increasing the Zn-precursor exposure time results in an improved ZnO coverage in AAO pores with a diameter of 65 nm (Elam *et al*. 2003 [22]. Reproduced with permission of American Chemical Society.). (b) Wall thickness measured along the length of a HfO_2 nanotube obtained by ALD of HfO_2 into an AAO template followed by dissolution of the template. (Perez *et al*. 2008 [23]. Reproduced with permission of Wiley.)

Perez *et al*. investigated the conformality of ALD processes in AAO by means of TEM [23]. After depositing a HfO_2 ALD layer into AAO structures and selective dissolution of the AAO, nanotubes could be obtained by replicating the AAO pores (Figure 1.12b). Using TEM, the conformality of the ALD process could be quantified by locally measuring the thickness of the replicated nanotube as a function of depth in the original AAO nanopore. Note that the diffusion-limited behavior of ALD in AAO pores can be exploited to achieve patterned ALD on the interior surface of an AAO membrane [95]. Adsorption of a first ALD precursor to a certain depth in the pore can block the active surface sites and prevent the subsequent adsorption of a second ALD precursor on that part of the pore walls, allowing for depth-controlled deposition. Using the passivation effect of TMA, ALD of ZnO, TiO_2, V_2O_5 has been achieved at controlled depths in AAO pores.

Under standard ALD conditions, the precursor vapor penetrates into microscopic holes or trenches through molecular flow (or Knudsen diffusion), because the mean free path of the precursor molecules is much larger than the diameter of the hole or the width of the trench. For instance, at 200 °C and a pressure of 1 Torr, the mean free path of the TMA molecules is about 35 μm. At sufficiently low pressure, molecular flow can also be achieved in macroscopic holes (Figure 1.15). Therefore, when ALD is performed at sufficiently low pressure, relatively simple test structures can be used to determine the depth of infiltration of ALD material into a structure with a given AR. Becker *et al*. introduced the use of fused-silica capillary tubes with a diameter of 20 μm to measure the conformality of ALD layers [96]. The tubes were exposed to an ALD process, heated to burn off the ALD coating on the outside, and filled with a fluid having a refractive index matching that of fused silica. By placing the tubes in an optical microscope, the depth of infiltration could be visually determined. The authors demonstrated successful ALD of WN in a capillary with an AR of about 200 : 1 (Figure 1.13a). Dendooven *et al*. introduced another macroscopic approach for quantifying the conformality of ALD [97, 98]. A macroscopic test structure was created by cutting a rectangular-shaped structure from a sheet of aluminum foil and clamping the resulting foil in between two silicon wafers (Figure 1.13b). This simple structure allowed for a direct and straightforward test of the ability of an ALD process to coat "around the corner." After deposition, the structure can be disassembled to inspect the deposition of material on the interior surface of the rectangular hole. A successful conformal coating with TiN is illustrated in Figure 1.13c, while a nonconformal Ru coating is shown in Figure 1.13d. The method was later extended by Musschoot *et al*. to investigate the penetration of thermal and plasma-enhanced ALD into fibrous materials [99].

The macroscopic test structures allow for quantitative analysis of the film thickness profile via spectroscopic ellipsometry (SE) measurements. Figure 1.14 shows the Al_2O_3 film thickness as a function of depth in a hole with an AR of about 200 : 1 for two TMA exposure times. As for the ZnO process shown in Figure 1.12a, the conformality could be improved by increasing the TMA exposure time. The experimental results depicted in Figure 1.12a,b show similar trends. The relative coverage or thickness is (nearly) at its maximum near the entrance of the hole/pore. At a certain depth, depending on the (unsaturated)

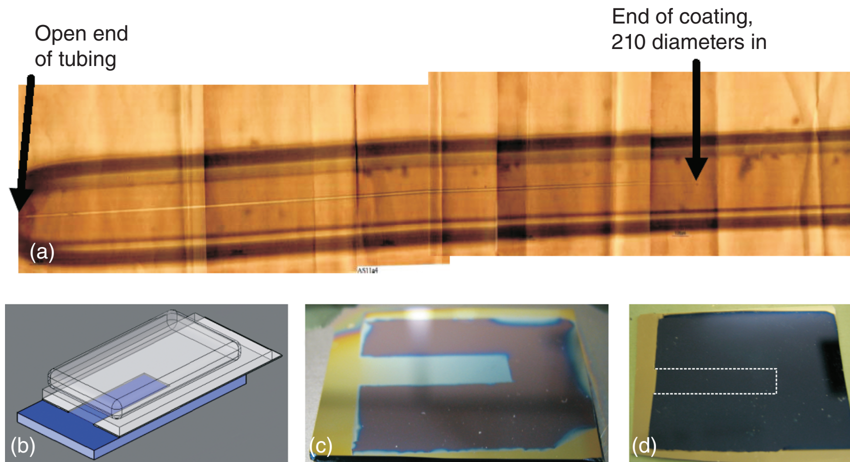

Figure 1.13 Macroscopic test structures that allow for visual inspection of the penetration depth of the ALD material. (a) WN coating inside a fused-silica capillary tube having an inner diameter of 20 μm. (Becker *et al*. 2003 [96]. Reproduced with permission of American Chemical Society.) (b) Schematic representation of a macroscopic hole with rectangular cross section (blue area) that can be disassembled into planar pieces of SiO_2 wafer after ALD. (c) The conformal deposition of TiN on the interior surface of a hole with an AR of 200 : 1 (defined as depth:width). In (d), the yellow coating outside of the cover is due to Ru deposition, while there is no coating inside the marked hole region, illustrating the lack of conformality for this Ru ALD process.

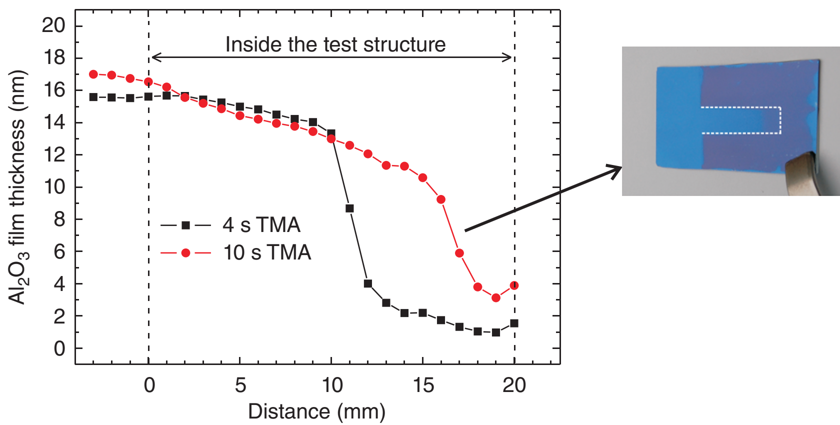

Figure 1.14 Film thickness profiles obtained for Al_2O_3 ALD in a macroscopic rectangular hole with an AR of 200 : 1. Increasing the TMA exposure time causes the Al_2O_3 coating to penetrate deeper into the test structure.

exposure time, the coverage or thickness gradually decreases as a function of depth in the hole/pore. The resulting data on film thickness as a function of penetration depth can be compared to simulations based on models for the diffusion of ALD precursors in deep holes or trenches (see the following discussion).

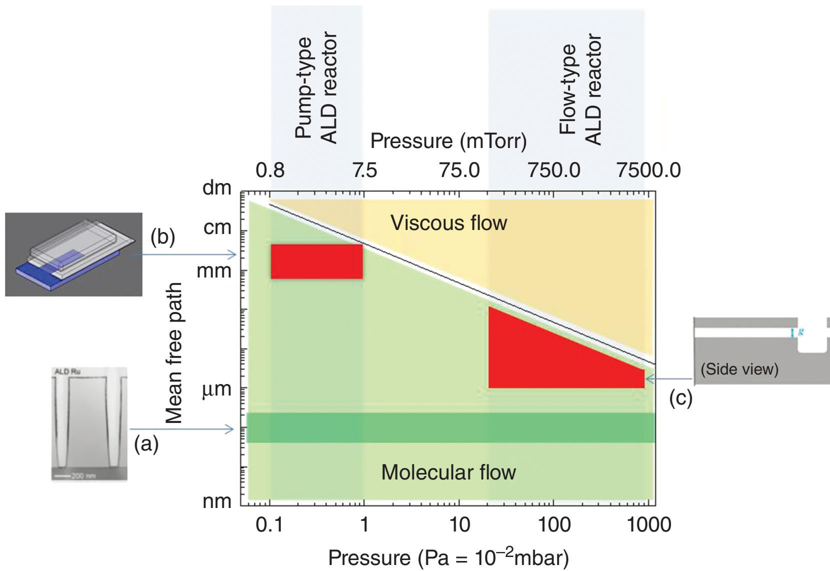

Figure 1.15 Mean free path of TMA molecules at 200 °C as a function of pressure in the ALD reactor. At all relevant pressures and for all relevant nano- and microstructures, precursor transport is governed by molecular flow. Different approaches have been developed for quantifying the conformality of ALD processes in different pressure regimes: (a) deposition into nano-sized features, followed by cross-sectional electron microscopy, (b) dedicated macroscopic lateral trench structures, as proposed by Dendooven *et al*. for low-pressure processes, and (c) dedicated micrometer-sized lateral trench structures as recently proposed by Puruunen *et al*. for high-pressure processes.

As illustrated in Figure 1.15, the approach using millimeter-sized macroscopic structures as proposed by Dendooven *et al.* is limited to low-pressure ALD processes as typically encountered in the pump-type ALD reactors that are used for PE-ALD research (where the chamber is evacuated by pumping in between half cycles). The more traditional flow-type ALD reactors (where the chamber is evacuated by purging in between half cycles) typically operate at significantly higher pressures, and at these pressures, the flow in millimeter-sized structures is determined by viscous flow conditions. Puurunen *et al.* recently proposed an approach using MEMS fabrication techniques to fabricate horizontal trenches with ARs up to 25 000:1 under thin membranes. After ALD, the thin membrane can be easily peeled off, and the deposited film can be investigated as a function of "depth" (in fact, lateral position) on the interior surface of the "trench" [100].

1.3.2 Modeling the Conformality of ALD

Gordon *et al.* [101] proposed an analytical model to predict the required exposure (defined as the product of precursor partial pressure present at the opening of the hole, P, and the precursor pulse duration, t) to conformally coat a cylindrical hole with a certain aspect ratio $AR = L/D$, with L being the depth and D the diameter

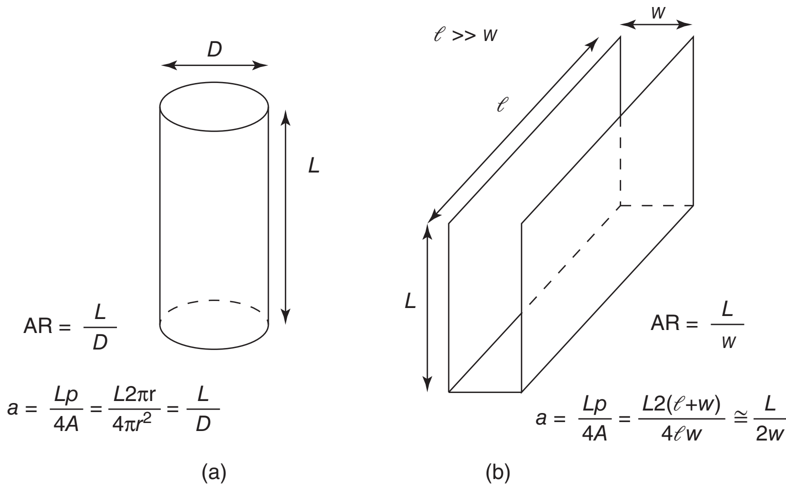

Figure 1.16 Aspect ratio (AR) and generalized aspect ratio (a) for a cylindrical hole (a) and a trench (b).

of the cylindrical hole (see also Figure 1.16):

$$P \cdot t = K_{\max} \sqrt{2\pi mkT} \cdot \left(1 + \frac{19}{4}a + \frac{3}{2}a^2\right) \quad (1.1)$$

In this equation, $K_{\max}$ is the saturated coverage per surface area (molecules per square meter), m is the mass of the precursor molecules, k is the Boltzmann constant, and T is the temperature. For large ARs, the required exposure increases approximately quadratically with a. The idea behind the model is schematically shown in Figure 1.17a. Saturation of the pore walls starts at the top part of the hole and then propagates as a "front" through the hole. It is assumed that the precursor molecules stick to the wall upon their first collision with an uncoated part of the wall, that is, the sticking probability is unity. For unsaturated exposures, the coverage profile consists of a fully saturated part that abruptly stops at the "front" position. Mathematically, the model can be derived using gas conductance equations: the fully covered part of the hole acts as a "tube" leading to the reactive uncoated part of the hole, which can be considered as a "vacuum pump." The authors showed good agreement between the predicted and the experimentally derived saturation dose for ALD of HfO_2, Ta_2O_5, WN, and V_2O_5 in cylindrical holes with a known AR [102].

Although the formulae used to develop Equation 1.1 were derived for cylindrical holes [103], Equation 1.1 can also (approximately) be applied for trenches and holes that have a noncircular cross section by introducing a generalized expression for a,

$$a = \frac{Lp}{4A}$$

where L is the depth of the hole, p its perimeter, and A its cross-sectional area. For cylindrical holes, a then still equals depth/diameter. For a trench of width w, the expression simplifies to $L/(2w)$, which is only half of the AR that is conventionally

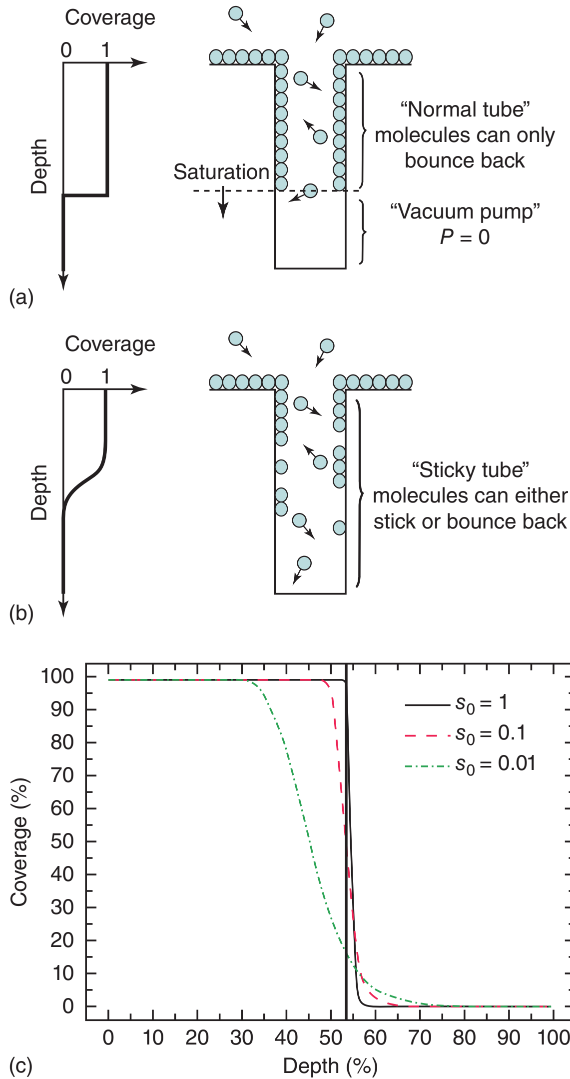

Figure 1.17 (a) Schematic representation of the idea behind the model proposed by Gordon *et al*. The resulting coverage profile is characterized by a step. (b) Schematic representation of the model proposed by Dendooven *et al*. The resulting coverage profile is characterized by a slope of decreasing thickness. (c) TMA coverage as a function of depth for a cylindrical hole with an AR of 100 : 1 for simulations with an initial sticking probability $s_0 = 1$, 0.1, and 0.001 ($P = 0.3$ Pa, $t = 5$ s, $K_{max} = 4.7 \times 10^{18}$ m^{-2}).

used for trenches, that is, L/w. Given that $(P{\cdot}t) \sim a^2$ for large ARs, the model thus predicts that a trench requires four times less exposure compared to a hole with the same AR (depth-to-width ratio).

During ALD in a nanoscopic hole, such as an AAO pore, the coating deposited during each ALD cycle decreases the pore diameter. Consequently, for a fixed unsaturated exposure, the Gordon model predicts a decrease in the penetration depth with each ALD cycle deposited. This gives rise to a slope of decreasing film thickness along the depth of the pore in the final film thickness profile, as also observed in the experimentally obtained profiles. Perez *et al*. showed good agreement between the slope obtained in the depth profiles for HfO_2 ALD in AAO pores (Figure 1.12b) and the slope predicted by iteratively applying

Gordon's model to a pore that is gradually getting clogged as the ALD process progresses. However, the slope observed in the thickness profiles for Al_2O_3 ALD in macroscopic holes (Figure 1.14) cannot be explained by an increasing AR during the deposition, because the deposited film thickness (typically a few nm) is negligible compared to the width of the hole (~100 μm). In this case, the observed slope is related to a sticking probability, which is less than 1 (as can be expected for any real ALD process).

Dendooven *et al*. extended the kinetic model of Gordon *et al*. for sticking probabilities of less than unity [97]. The extended model is based on conductance formulae that were derived for a "sticky" tube [104]. In this case, the precursor molecules can either stick on an uncoated part of the wall or bounce back from it (Figure 1.17b). Moreover, the sticking probability on a reactive part of the wall is assumed to decrease linearly with increasing surface coverage according to Langmuir's law. Figure 1.17c shows the effect of the initial sticking probability, s_0, on the simulated coverage profile for a cylindrical hole with an AR of 100 : 1. For $s_0 = 100\%$, a step-like profile is obtained, in agreement with the model by Gordon *et al*. For lower values of s_0, a slope of decreasing thickness is predicted. Using an initial sticking probability of 10% for TMA, good agreement was achieved between the simulated and the experimentally obtained Al_2O_3 thickness profiles.

Elam *et al*. developed a one-dimensional (1D) Monte Carlo (MC) model for simulating experimental Zn coverage profiles obtained by cross-sectional analysis of ZnO layers deposited by ALD in AAO membranes [22] (Figure 1.12a). Based on their 1D MC model, Elam *et al*. predicted a reaction-limited behavior rather than a diffusion-limited behavior for sufficiently low reaction probabilities and reasonable ARs. This classification between diffusion- and reaction-limited regimes was later confirmed by Dendooven *et al*. [105] and Knoops *et al*. [106] Figure 1.18 shows the pressure evolution and coverage evolution in a rectangular hole with an AR of 66 : 1 for an initial sticking probability of 10%. In this case, the deposition is clearly diffusion-limited. With progressing time, the precursor molecules penetrate deeper into the hole, leading to a moving deposition "front" toward the bottom of the hole. On the other hand, if an initial sticking probability of 0.1% is used in the simulation, the deposition becomes reaction-limited. From the very start of the exposure, a large fraction of the precursor molecules can reach the bottom of the hole, but the reaction is slow as observed in the coverage profile evolution.

1.3.3 The Conformality of Plasma-Enhanced ALD

As mentioned earlier, achieving a good conformality in high AR structures is considered to be more challenging for PE-ALD than for thermal ALD. This is because radicals can recombine upon collision with a surface. For instance, an oxygen radical can recombine with an oxygen atom that resides at the surface to form molecular O_2, which is often nonreactive to the adsorbed metal precursor on the surface. When coating deep holes or trenches with PE-ALD, the reactive species have to undergo multiple wall collisions during which they may be lost through surface recombination before they can reach the surfaces deeper in the hole. It

is therefore inevitable that the elimination of radicals through recombination on the sidewalls of high AR structures will limit the conformality of PE-ALD.

The recombination probability r describes the probability that a reactive atom (radical) will recombine upon collision with a surface and is typically determined

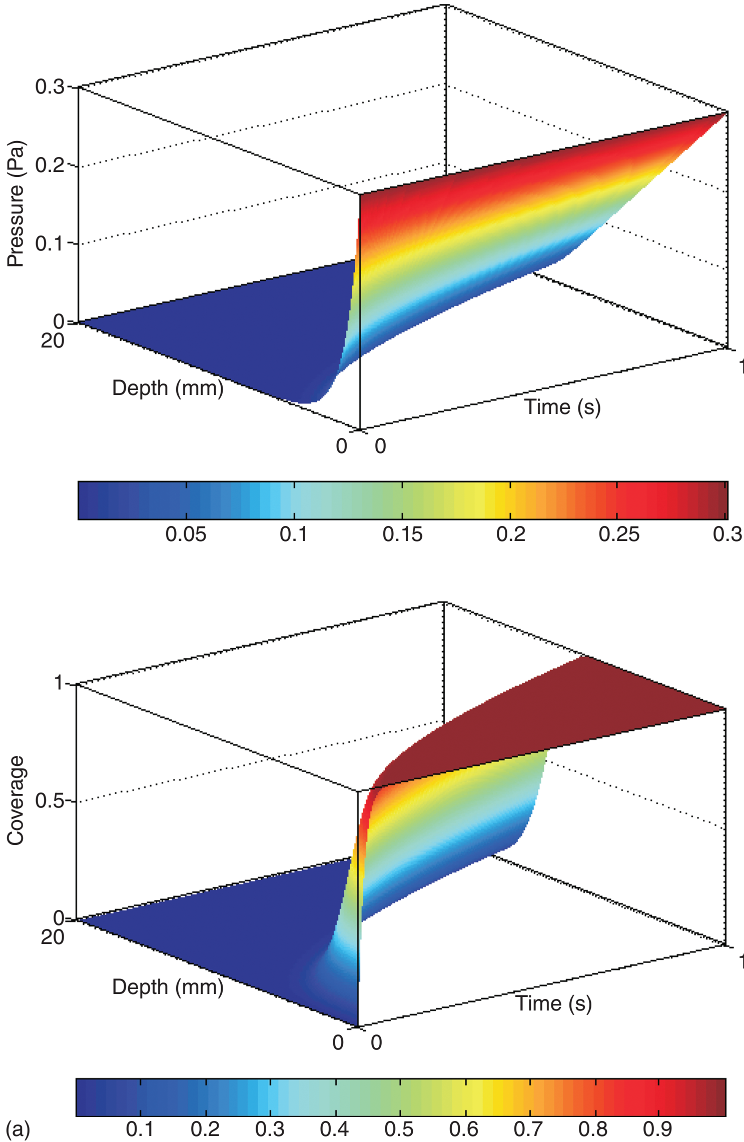

Figure 1.18 Simulated pressure (a) and coverage (b) profiles calculated for a TMA pulse in a rectangular hole with an AR of 66 : 1 ($P = 0.3$ Pa, $t = 1$ s, $K_{max} = 4.7 \times 10^{18}$ m^{-2}). For panel (a), the initial sticking probability was 10%, resulting in a diffusion-limited deposition behavior. For panel (b), the initial sticking probability was 0.1%, resulting in a reaction-limited deposition behavior.

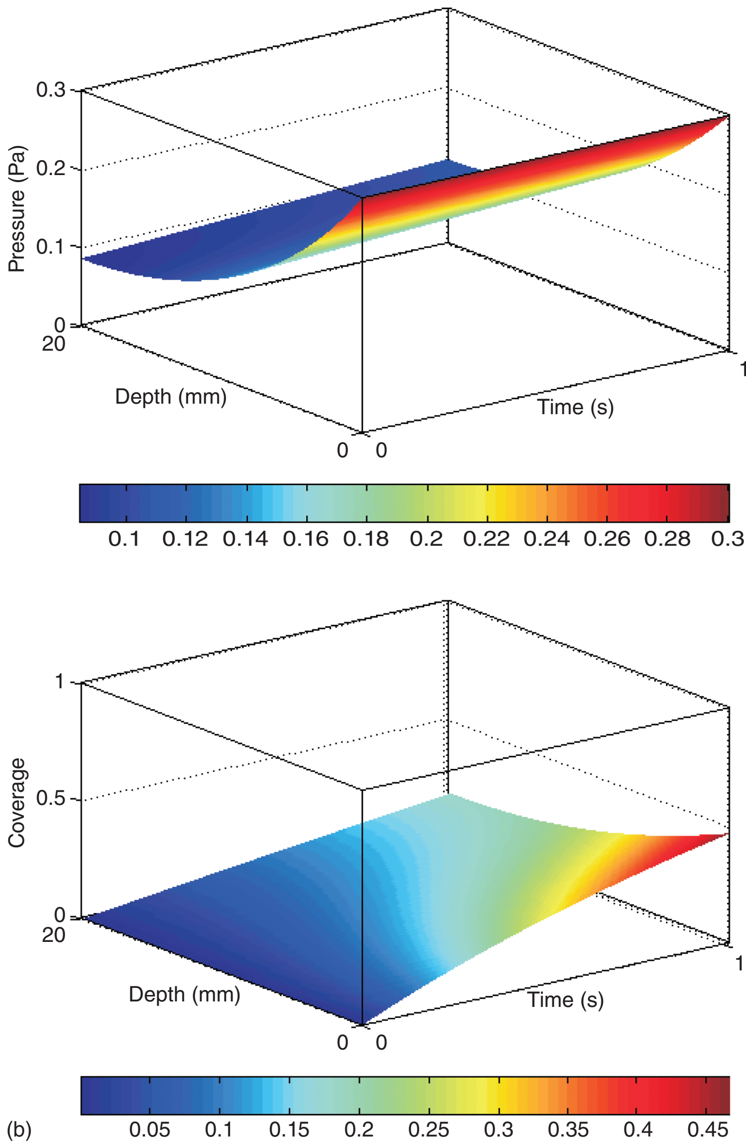

Figure 1.18 (*Continued*).

for a certain atom type on a certain surface material. Reported values for recombination probabilities of O, N, and H atoms on various surfaces span a large range, from 0.000094 for the recombination of O atoms on Pyrex to 0.8 for the recombination of H atoms on silicon [106]. There is quite a discrepancy in the *r* values published in the literature. This is likely related to the large variety of (often indirect) techniques that have been used to monitor atom recombination (including actinometric OES, two-photon laser-induced fluorescence, use of dual thermocouples, or catalytic probes, and mass spectroscopy) [107, 108]

and to the fact that the atom recombination coefficient depends not only on the surface material but also on the surface conditions (e.g., presence of impurities, adsorbed gas species, certain surface pretreatments), the gas pressure and temperature, the surface temperature, and the plasma configuration [109–112]. This latter issue has, among others, been addressed by Cartry *et al.*, who measured a value of 0.0004 for O atom recombination on a silica surface positioned in the afterglow region of a microwave plasma, while a two orders of magnitude higher value of 0.03 was obtained on a silica surface directly submitted to the plasma [113]. A possible explanation for this difference is that ions (which are predominantly present in the core of the plasma) can create active sites for surface recombination. As mentioned earlier, the gas pressure can also affect the recombination probability. Adams *et al.* reported a decreasing N atom recombination with increasing pressure for silicon, aluminum, and stainless steel surfaces. For instance, on silicon, they measured a recombination probability of 0.0026 at 1 Torr, 0.0016 at 3 Torr, and 0.0005 at 5 Torr. Gomez *et al.* observed a similar trend for O atom recombination [111]. Moreover, significant dependencies on the surface temperature can exist. For instance, Guyon *et al.* measured an increase in the O atom recombination probability on alumina from 0.0097 at room temperature to 0.061 at 500 °C [114]. On the other hand, Wood and Wise reported quasi-constant H atom recombination on several metals over a large range of temperatures [115]. It is learned from the given overview that the conformality of a PE-ALD process will depend, via the recombination probability, on the type of radicals used as reactant in the process, on the material that is deposited, and on the process parameters such as the gas pressure, deposition temperature, and plasma configuration. Note that the gas pressure and the plasma configuration not only affect the recombination probability but also the radical density at the sample surface and the entrance of high AR structures, which in turn will have an effect on the conformality. Furthermore, the recombination coefficient will likely vary over the duration of a plasma exposure, because the sample surface changes (due to reaction with the radicals) from a surface that is covered with metal precursor ligands to the oxide, nitride, or metal that is being deposited.

There exist only a few systematic studies on the conformality of PE-ALD in the literature. Dendooven *et al.* used macroscopic test structures to study the influence of the gas pressure, the RF power, the plasma exposure time, and the directionality of the plasma plume on the conformality of the remote PE-ALD of Al_2O_3 from TMA and O_2 plasma [98]. To investigate the effect of the plasma type on the conformality, they compared the conformality of Al_2O_3 to the conformality of AlN deposited from TMA and NH_3 plasma. In addition, a Monte Carlo (MC) model was used to evaluate the effect of radical recombination. For the Al_2O_3 process using O_2 plasma, conformal coatings in holes with an AR of 40 : 1 (defined as depth/width) were achievable by optimizing the process parameters. The conformality of the AlN process was more limited, and an AR of 20 : 1 already seemed impractical. This suggests that the radicals generated in the NH_3 plasma suffer from faster recombination compared to the O radicals. The conformality of the Al_2O_3 PE-ALD process could be improved by increasing the radical density via the gas pressure or the RF power or by prolonging the plasma exposure

time. It should be noted that the H_2O formed as reaction product during the combustion reaction that takes place during the O_2 plasma step contributed to the apparent conformality of PE-ALD processes via a secondary thermal ALD reaction.

Knoops *et al*. used an MC model to obtain insights into the effect of the recombination probability *r* on the conformality of PE-ALD processes in high AR trenches. The required saturation dose increases considerably with increasing *r* values, especially for high ARs. Therefore, besides the diffusion-limited and reaction-limited regimes that are also observed in thermal ALD, they distinguished a recombination-limited regime for PE-ALD processes with high *r* values (or lower *r* values in combination with high ARs). It was further speculated that conformal coating in trenches with an AR of 30 : 1 should be achievable for PE-ALD processes with low *r* values. On the other hand, for high surface recombination probabilities, as observed on many metallic surfaces, impractically large exposures seem to be required to coat trenches with ARs larger than 10 : 1.

Kariniemi *et al*. verified the conformality of various PE-ALD processes by deposition into deep microscopic trenches and subsequent characterization by cross-sectional SEM [48]. They showed good conformality of metal oxide coatings deposited in trenches with ARs considerably larger than what had been achieved earlier (up to 60 : 1). The key difference with other remote PE-ALD studies [116–118] are the reactor design and, related to that, the two to three orders of magnitude higher pressures used during the O_2 plasma step. Compared to the inductively coupled RF plasma sources, the remote capacitively coupled RF plasma configuration used by Kariniemi *et al.* is expected to result in higher radical densities at the sample surface and the entrance of the trench and thus also in higher radical fluxes deeper in the trench and improved conformality. In addition, it is possible that a higher pressure during the plasma exposure causes the O radicals to recombine less efficiently at the trench walls. In the case of Ag PE-ALD using H_2 plasma, Kariniemi *et al.* observed Ag growth near the bottom of a 60 : 1 trench, but the coating was far from conformal. This can be related to the rather high recombination probability typically observed for H radicals on metals and/or to the absence of a secondary thermal ALD reaction contributing to the conformality.

Increasing the radical exposure, via the radical density available at the entrance of the hole or the exposure time, is found to be the key factor in improving the conformality of PE-ALD processes. The influence of the radical density was demonstrated in the work of Dendooven *et al*. by increasing the gas pressure and the RF power and in the work of Kariniemi *et al*. by modifying the plasma configuration. This latter method appears to be more effective.

The experimental results also show that reasonable ARs can be achieved for O_2-based PE-ALD processes. The MC model of Knoops *et al*. solely attributes this to the relatively low recombination probability of O radicals on oxide surfaces. However, the experimental film thickness profiles obtained for PE-ALD of Al_2O_3 by Dendooven *et al*. and Musschoot *et al*. could only be "reproduced" by MC simulations if a superposition of two reactions was assumed, that is, (i) combustion reactions of O radicals with adsorbed TMA molecules at the entrance

of the hole and (ii) a secondary thermal ALD reaction of H_2O molecules that are being generated during the combustion reactions with adsorbed TMA molecules deeper in the hole. On the other hand, Kariniemi *et al*. concluded that the secondary H_2O effect plays a minor role in their depositions as good conformality was also achieved for the SiO_2 process, while the Si precursor reacts only slowly with H_2O. This might be explained by the difference in radical fluxes inside the high AR structures. Indeed, for sufficiently large O radical fluxes, as is also the case for planar substrates, the effect of the secondary H_2O reaction will be minor as it has to compete with the combustion-like O radical reactions, which are likely to occur faster. If the radical flux is low, secondary reactions with the H_2O will have a relatively larger impact.

When NH_3, N_2, or H_2 plasmas are used, H_2O is usually not formed as a reaction product in the plasma step, and secondary thermal ALD reactions are not expected. The results by Dendooven *et al*. demonstrated that the growth of nitrides in high AR structures using NH_3 plasma is not trivial, pointing to a high recombination probability of the radicals generated in the plasma. The chemistry of a NH_3 plasma is, however, very complex, and an understanding of the surface recombination of its radicals remains elusive [119]. Even for the pure N_2 plasma, there are only a few studies concerning the surface recombination of N radicals. Although not stated explicitly in the literature, the lack of papers reporting conformal growth of nitrides with PE-ALD using NH_3 or N_2 plasma could indicate that it is indeed challenging to achieve good conformality for those processes.

1.3.4 Conformal Coating of Nanoporous Materials

ALD in combination with nanoporous materials and membranes allows for the creation of nanomaterials with improved compositional and structural properties through either replication or coating of the porous network. These materials have applications in photonics, catalysis, gas separation, green energy conversion, sensing, and so on. The unique potential of ALD to conformally coat mesopores was demonstrated in 1996 for SnO_2 ALD in porous silicon [87]. Since then, many authors have used ALD in porous films and membranes to fabricate nanostructures, to functionalize the pore walls, or to tune the pore size.

The first freestanding nanotubes realized by ALD were fabricated by the infiltration of a polycarbonate filter (200 nm diameter pores) with TiO_2 or ZrO_2 followed by the dissolution of the filter [120]. Later, several groups have used AAO (typically 30–500-nm pores) as a dissoluble template for the fabrication of nanotubes (Figure 1.19) [123–126]. For instance, Daub *et al*. synthesized ferromagnetic Ni nanotubes by ALD of Ni oxide in the pores of an AAO template followed by reduction of the metal oxide in hydrogen atmosphere [121]. Bae *et al*. demonstrated the possibility of producing coaxial nested TiO_2 nanotubes by introducing dissoluble Al_2O_3 spacer layers between two or more TiO_2 coatings in an AAO template [127]. Gu *et al*. applied the same trick to synthesize multiwalled HfO_2 nanotubes [122]. Furthermore, several authors have investigated the photocatalytic activity of TiO_2 nanotube arrays created by TiO_2 ALD in AAO templates [128–130].

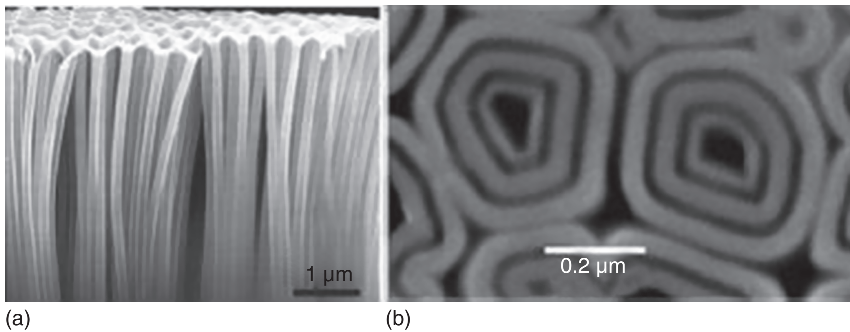

Figure 1.19 (a) SEM image of freestanding TiO_2/Ni/TiO_2 nanotubes obtained via ALD in an AAO template. (Daub *et al*. 2007 [121]. Reproduced with permission of American Institute of Physics.) (b) Top view SEM image of triple coaxial HfO_2 nanotubes obtained by using AAO and Al_2O_3 ALD layers as template and spacer layers, respectively. (Gu 2010 [122]. Reproduced with permission of American Chemical Society.)

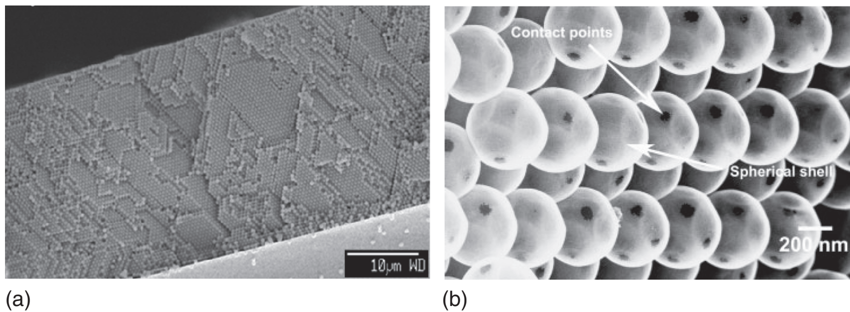

Figure 1.20 (a) SEM image of an opal film. (Karuturi *et al*. 2010 [138]. Reproduced with permission of American Chemical Society.) (b) SEM image of a TiO_2 inverse opal synthesized by ALD. (King *et al*. 2005 [132]. Reproduced with permission of Wiley.)

ALD has also been used for infiltration and replication of opal structures made of close-packed colloidal silica or polystyrene spheres [131–138]. Opal replicas, or inverse opals, thus consist of a regular arrangement of submicrometer air voids embedded in a solid matrix material. Because of their periodically modulated dielectric constant, these structures can exhibit a photonic band gap (photon wavelengths for which wave propagation is not possible inside the material) and are therefore promising candidates as 3D photonic crystals. Figure 1.20 shows an opal structure consisting of 510-nm polystyrene particles. It is clear that only a highly conformal deposition method such as ALD can achieve uniform infiltration of the opal film. Successful replication of an opal structure by means of TiO_2 ALD and subsequent etching of the silica spheres could be demonstrated.

Most research has focused on ALD coatings in materials with pore sizes >30 nm, for example, using the aforementioned Si-based trench structures, AAO and opal structures. Fewer studies have focused on ALD coatings in sub-10 nm pores. George and coworkers investigated ALD of Al_2O_3, TiO_2, and SiO_2 in 5-nm tubular alumina membranes [78, 139]. In each ALD half cycle, the pore

diameter was derived from *in situ* N_2 conductance measurements (assuming Knudsen flow in the pores). The pore size was smaller after a precursor exposure than after the subsequent H_2O exposure, in accordance with the replacement of the bulky precursor ligands on the pore walls by the smaller OH groups during the H_2O step. The pore diameter was successfully reduced to molecular diameters (estimated in the range 3–10 Å), demonstrating the potential of ALD to tailor nanoporous membranes for specific gas separation purposes. Lin and coworkers used ALD of Al_2O_3 to modify sol–gel prepared alumina membranes with 4 nm pores [140, 141]. ALD resulted in an improved separation of water vapor over O_2 gas via the capillary condensation mechanism. McCool and DeSisto studied the pore size reduction of a mesoporous silica membrane via catalyzed ALD of SiO_2 [142, 143]. For a sufficient number of ALD cycles, the temperature dependence of the N_2 permeance through the membrane revealed a shift from Knudsen to configurational diffusion, suggesting pore sizes in the microporous regime [144]. Separation experiments with H_2 and CH_4 also showed deviation from the Knudsen diffusion mechanism in the direction of molecular sieving. Velleman *et al.* combined pore size tuning of AAO membranes by ALD with wet chemical functionalization of the coated membrane [145]. The surface modification with highly hydrophobic silane species was employed to improve the selectivity of the membrane for hydrophobic molecules. Due to hydrophobic–hydrophilic repulsions, the chemically modified membrane showed enhanced sensitivity to the transport of hydrophobic molecules over hydrophilic molecules. Chen *et al.* performed ALD of TiO_2 to reduce the pore size of kinked silica nanopores from 2.6 to 2 nm [146]. The authors demonstrated great potential of this structure for DNA sequencing.

In a series of recent papers, Dendooven *et al.* explored the limit of ALD for coating the interior surface of nano-sized pores. They used meso- and microporous SiO_2 and TiO_2 films that were deposited onto silicon substrates. Because of the well-defined sample structure, ALD into the nanoporous layers could be monitored *in situ* using XRF, GISAXS [80], and EP [79].

A first series of experiments focused on ALD into mesoporous silica thin films consisting of an unordered 3D network of silica nanoslabs, with controllable average pore diameters in the range of 6–20 nm. The films exhibited high porosity (70–80%) and excellent 3D pore accessibility. Figure 1.21 summarizes the results obtained for ALD of TiO_2 from tetrakis(dimethylamino) titanium (TDMAT) and H_2O in the 3D mesoporous network of nanoslab-based silica thin films [79, 147]. The ALD conditions for reaching saturation in the mesoporous films were investigated via determination of the chemical composition using *in situ* XRF. Films were successively exposed to 1 s TDMAT pulses, each of them followed by 20 s XRF data collection. The Ti XRF intensity (Ti Kα peak area), which is proportional to the amount of Ti atoms deposited in the mesoporous thin film, is plotted against the TDMAT exposure time in Figure 1.21b. About 4 s of exposure was needed to reach saturation. Prolongation of the exposure up to 20 s did not significantly enhance the uptake. It is concluded that the penetration of the ALD precursor proceeds readily in the 3D network of interconnected channels. Exposure of a mesoporous thin film to repeated cycles of the TDMAT/H_2O ALD process is expected to result in the conformal

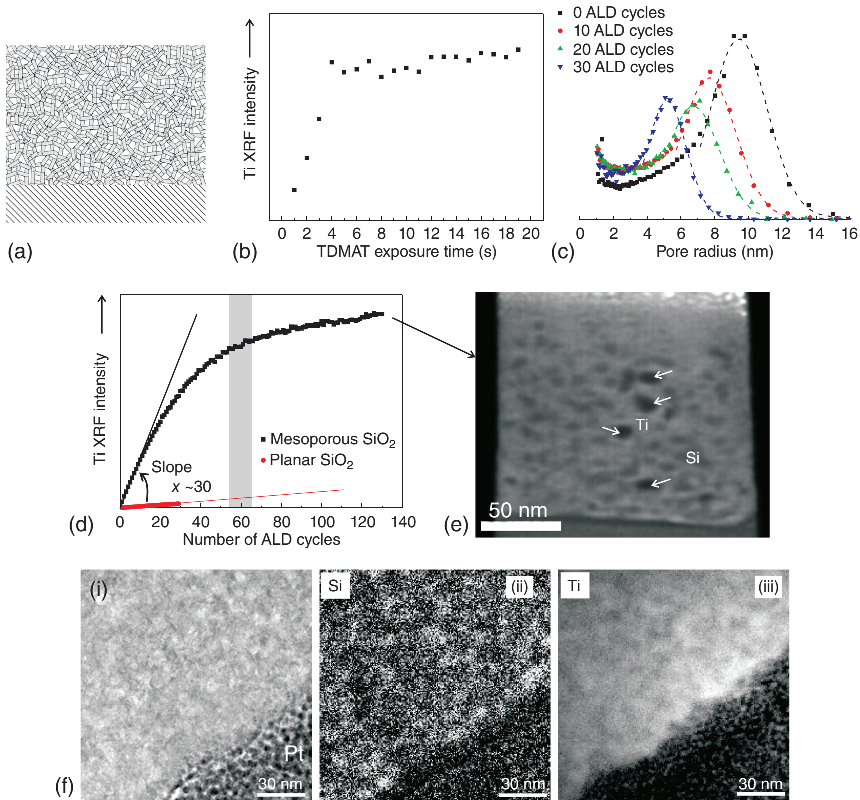

Figure 1.21 TiO_2 ALD in mesoporous silica thin films. (a) Schematic representation of the nanoslab-based mesoporous films. (b) Ti XRF intensity as a function of the TDMAT exposure time on a 115-nm-thick film with about 6.5 nm pores and about 75% porosity. (c) Pore radius distribution calculated from *in situ* EP data measured every 10 ALD cycles on a 150-nm thick film with about 18 nm pores and about 80% porosity. (d) Ti XRF intensity against the number of ALD cycles on a 120-nm film with about 7.5 nm pores and about 75% porosity and on a planar SiO_2 substrate. (e) Electron tomography study of the TiO_2-coated film in (d): out-of-plane orthoslice through the 3D reconstruction of a micropillar sample. Dark gray, silica; light gray, TiO_2; and black (arrows), voids. (f) TEM image of a cross-sectional sample of the TiO_2-coated silica film (i), Si energy-filtered TEM map of this region (ii), and Ti energy-filtered TEM map of this region (iii).

deposition of a TiO_2 film on its pore walls and thus in a reduction of its pore size. Figure 1.21c confirms a gradual decrease in pore radius with each 10 ALD cycles deposited in channel-like mesopores with an initial average pore radius of about 9 nm. It should be noted that the pore radius reduction was not only caused by the ALD coating but also influenced by shrinkage of the porous network during ALD. Figure 1.21d shows the Ti uptake against the number of ALD cycles in a film with an initial average pore diameter of about 7.5 nm. In an ALD process performed on a planar reference substrate, the XRF intensity increased linearly with the number of ALD cycles, as expected. XRR revealed a growth rate of 0.5 Å per cycle on the planar substrate. During ALD on the mesoporous film,

the slope of the XRF intensity curve was initially much larger, proving that TiO_2 got deposited onto the interior surface of the channel-like mesopores. The slope decreased gradually with the number of ALD cycles because the TiO_2 coating on the pore walls caused a gradual decrease in the pore diameter and, related to that, a decline in the interior surface area of the porous network. Evidently, the amount of Ti atoms deposited per ALD cycle is directly linked to the available surface area. Finally, the slope of the Ti XRF intensity curve became constant, suggesting that the pores were no longer accessible for the TDMAT molecules and that deposition continued on top of the filled mesoporous film. Shrinking the pore diameter below the estimated kinetic diameter of the TDMAT molecule, 0.7 nm [148], took about 60 ALD cycles, indicating a diameter decrease by 0.11 nm per cycle. The TiO_2 growth rate in the pores was thus about 0.55 Å per cycle, which is in reasonable agreement with the value found for deposition on the planar substrate (0.5 Å per cycle). The TiO_2-filled mesoporous silica film was further investigated by electron tomography. Figure 1.21e shows an out-of-plane orthoslice through the 3D reconstruction. The result confirms the deposition of TiO_2 throughout the whole film. It furthermore revealed the presence of larger pores (diameter >7.5 nm) that were not completely filled with TiO_2 ALD. These pores most likely became inaccessible for the ALD precursors due to filling of the smaller pores. Elemental distribution maps from energy-filtered TEM confirmed the presence of TiO_2 throughout the mesoporous silica film (Figure 1.21f). Similar results were obtained for ALD of TiO_2 and HfO_2 into mesoporous TiO_2 with ink-bottle-shaped mesopores [86, 149].

Dendooven *et al.* also studied the conformal deposition within microporous silica films with an average pore size of about 1 nm [81]. TDMAT molecules have a molecular diameter of about 0.7 nm and therefore managed to penetrate into the micropores of this film (Figure 1.22a). After application of one ALD cycle, about 18 times more Ti atoms were deposited in the microporous film than on a planar reference substrate (Fig. 1.22(b)). The increment of Ti loading became lower during the subsequent ALD cycles, as the micropores became too narrow after 1–3 cycles of TiO_2 deposition and were no longer accessible for the TDMAT molecules.

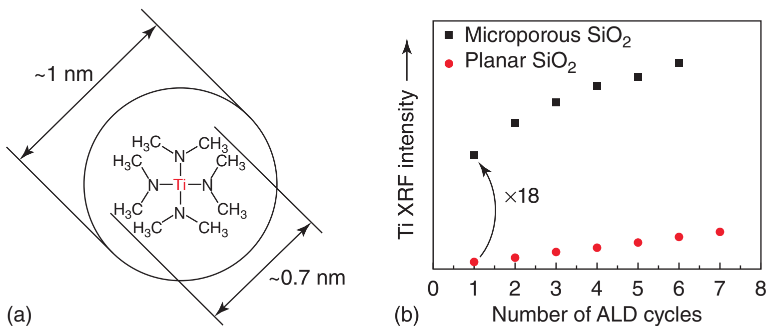

Figure 1.22 TiO_2 ALD in a microporous silica thin film with a porosity of about 40% and a thickness of about 80 nm. (a) Size of the TDMAT molecule as compared to the average pore size. (b) Ti XRF intensity against the number of ALD cycles on the microporous film and a planar SiO_2 substrate.

This systematic study clearly demonstrates the ability of ALD to deposit conformal coatings on the pore walls of both channel-like and ink-bottle-shaped mesopores with diameters in the low mesoporous and even microporous regime, indicating that ALD is ideally suited for conformal deposition into porous materials and for atomic level tuning of the pore size down to near molecular dimensions.

References

1 George, S.M. (2010) *Chem. Rev.*, **110**, 111–131.
2 Leskelä, M., Ritala, M., and Nilsen, O. (2011) *MRS Bull.*, **36**, 877–884.
3 Puurunen, R.L. (2005) *J. Appl. Phys.*, **97**, 121301.
4 Miikkulainen, V., Leskelä, M., Ritala, M., and Puurunen, R.L. (2013) *J. Appl. Phys.*, **113**, 021301.
5 Detavernier, C., Dendooven, J., Sree, S.P., Ludwig, K.F., and Martens, J.A. (2011) *Chem. Soc. Rev.*, **40**, 5242–5253.
6 Park, M.H., Jang, Y.J., Sung-Suh, H.M., and Sung, M.M. (2004) *Langmuir*, **20**, 2257–2260.
7 Chen, R., Kim, H., McIntyre, P.C., Porter, D.W., and Bent, S.F. (2005) *Appl. Phys. Lett.*, **86**, 191910.
8 Chen, R. and Bent, S.F. (2006) *Adv. Mater.*, **18**, 1086.
9 Sinha, A., Hess, D.W., and Henderson, C.L. (2006) *J. Electrochem. Soc.*, **153**, G465–G469.
10 Farm, E., Kemell, M., Ritala, M., and Leskelä, M. (2008) *J. Phys. Chem. C*, **112**, 15791–15795.
11 Mackus, A.J.M., Mulders, J.J.L., van de Sanden, M.C.M., and Kessels, W.M.M. (2010) *J. Appl. Phys.*, **107**, 116102.
12 Lee, W., Dasgupta, N.P., Trejo, O., Lee, J.-R., Hwang, J., Usui, T., and Prinz, F.B. (2010) *Langmuir*, **26**, 6845–6852.
13 Kim, W.-H., Lee, H.-B.-R., Heo, K., Lee, Y.K., Chung, T.-M., Kim, C.G., Hong, S., Heo, J., and Kim, H. (2011) *J. Electrochem. Soc.*, **158**, D1–D5.
14 Okuyama, Y., Barelli, C., Tousseau, C., Park, S., and Senzaki, Y. (2005) *J. Vac. Sci. Technol., A*, **23**, L1–L3.
15 Granneman, E., Fischer, P., Pierreux, D., Terhorst, H., and Zagwijn, P. (2007) *Surf. Coat. Technol.*, **201**, 8899–8907.
16 Poodt, P., Cameron, D.C., Dickey, E., George, S.M., Kuznetsov, V., Parsons, G.N., Roozeboom, F., Sundaram, G., and Vermeer, A. (2012) *J. Vac. Sci. Technol., A*, **30**, 010802.
17 Knez, M., Nielsch, K., and Niinistö, L. (2007) *Adv. Mater.*, **19**, 3425–3438.
18 Kim, H., Lee, H.-B.-R., and Maeng, W.-J. (2009) *Thin Solid Films*, **517**, 2563–2580.
19 Bae, C., Shin, H., and Nielsch, K. (2011) *MRS Bull.*, **36**, 877–884.
20 Elam, J.W., Dasgupta, N.P., and Prinz, F.B. (2011) *MRS Bull.*, **36**, 899–906.
21 Marichy, C., Bechelany, M., and Pinna, N. (2012) *Adv. Mater.*, **24**, 1017–1032.

22 Elam, J.W., Routkevitch, D., Mardilovich, P.P., and George, S.M. (2003) *Chem. Mater.*, **15**, 3507–3517.

23 Perez, I., Robertson, E., Banerjee, P., Henn-Lecordier, L., Son, S.J., Lee, S.B., and Rubloff, G.W. (2008) *Small*, **4**, 1223–1232.

24 Banerjee, P., Perez, I., Henn-Lecordier, L., Lee, S.B., and Rubloff, G.W. (2009) *Nat. Nanotechnol.*, **4**, 292–296.

25 Kucheyev, S.O., Biener, J., Wang, Y.M., Baumann, T.F., Wu, K.J., van Buuren, T., Hamza, A.V., Satcher, J.H., Elam, J.W., and Pellin, M.J. (2005) *Appl. Phys. Lett.*, **86**, 083108.

26 Elam, J.W., Libera, J.A., Pellin, M.J., Zinovev, A.V., Greene, J.P., and Nolen, J.A. (2006) *Appl. Phys. Lett.*, **89**, 053124.

27 Biener, J., Baumann, T.F., Wang, Y., Nelson, E.J., Kucheyev, S.O., Hamza, A.V., Kemell, M., Ritala, M., and Leskelä, M. (2007) *Nanotechnology*, **18**, 055303.

28 Ghosal, S., Baumann, T.F., King, J.S., Kucheyev, S.O., Wang, Y., Worsley, M.A., Biener, J., Bent, S.F., and Hamza, A.V. (2009) *Chem. Mater.*, **21**, 1989–1992.

29 Hakim, L.F., George, S.M., and Weimer, A.W. (2005) *Nanotechnology*, **16**, S375–S381.

30 King, D.M., Spencer, J.A. II, Liang, X., Hakim, L.F., and Weimer, A.W. (2007) *Surf. Coat. Technol.*, **201**, 9163–9171.

31 Hakim, L.F., Vaughn, C.L., Dunsheath, H.J., Carney, C.S., Liang, X., Li, P., and Weimer, A.W. (2007) *Nanotechnology*, **18**, 345603.

32 King, D.M., Liang, X., Zhou, Y., Carney, C.S., Hakim, L.F., Li, P., and Weimer, A.W. (2008) *Powder Technol.*, **183**, 356–363.

33 Zhou, Y., King, D.M., Li, J., Barrett, K.S., Goldfarb, R.B., and Weimer, A.W. (2010) *Ind. Eng. Chem. Res.*, **49**, 6964–6971.

34 Longrie, D., Deduytsche, D., and Detavernier, C. (2014) *J. Vac. Sci. Technol., A*, **32**, 010802.

35 Min, B., Lee, J., Hwang, J., Keem, K., Kang, M., Cho, K., Sung, M., Kim, S., Lee, M.-S., Park, S., and Moon, J. (2003) *J. Cryst. Growth*, **252**, 565–569.

36 Kang, M., Lee, J.-S., Sim, S.-K., Min, B., Cho, K., Kim, H., Sung, M.-Y., Kim, S., Song, S.A., and Lee, M.-S. (2004) *Thin Solid Films*, **466**, 265–271.

37 Fan, H.J., Knez, M., Scholz, R., Nielsch, K., Pippel, E., Hesse, D., Zacharias, M., and Gösele, U. (2006) *Nat. Mater.*, **5**, 627–631.

38 Law, M., Greene, L.E., Radenovic, A., Kuykendall, T., Liphardt, J., and Yang, P. (2006) *J. Phys. Chem. B*, **110**, 22652–22663.

39 Peng, Q., Sun, X.-Y., Spagnola, J.C., Hyde, G.K., Spontak, R.J., and Parsons, G.N. (2007) *Nano Lett.*, **7**, 719–722.

40 Hyde, G.K., Park, K.J., Stewart, S.M., Hinestroza, J.P., and Parsons, G.N. (2007) *Langmuir*, **23**, 9844–9849.

41 Lee, S.-M., Pippel, E., Gösele, U., Dresbach, C., Qin, Y., Chandran, C.V., Brauniger, T., Hause, G., and Knez, M. (2009) *Science*, **324**, 488–492.

42 Roth, K.M., Roberts, K.G., and Hyde, G.K. (2010) *Text. Res. J.*, **80**, 1970–1981.

43 Figure courtesy of A. Delabie, private communication.

44 Dendooven, J., Ramachandran, R.K., Devloo-Casier, K., Rampelberg, G., Filez, M., Poelman, H., Marin, G.B., Fonda, E., and Detavernier, C. (2013) *J. Phys. Chem. C*, **117**, 20557–20561.
45 George, S.M., Ott, A.W., and Klaus, J.W. (1996) *J. Phys. Chem.*, **100**, 13121.
46 Profijt, H.B., Potts, S.E., van de Sanden, M.C.M., and Kessels, W.M.M. (2011) *J. Vac. Sci. Technol., A*, **29**, 050801.
47 Profijt, H.B., Kudlacek, P., van de Sanden, M.C.M., and Kessels, W.M.M. (2011) *J. Electrochem. Soc.*, **158**, G88–G91.
48 Kariniemi, M., Niinistö, J., Vehkamäki, M., Kemell, M., Ritala, M., Leskelä, M., and Putkonen, M. (2012) *J. Vac. Sci. Technol., A*, **30**, 01A115.
49 Potts, S.E., Keuning, W., Langereis, E., Dingemans, G., van de Sanden, M.C.M., and Kessels, W.M.M. (2010) *J. Electrochem. Soc.*, **157**, P66–P74.
50 Heil, S.B.S., van Hemmen, J.L., van de Sanden, M.C.M., and Kessels, W.M.M. (2008) *J. Appl. Phys.*, **103**, 103302.
51 Rai, V.R., Vandalon, V., and Agarwal, S. (2010) *Langmuir*, **26**, 13732–13735.
52 Rai, V.R. and Agarwal, S. (2009) *J. Phys. Chem. C*, **113**, 12962–12965.
53 Kim, H. and Rossnagel, S.M. (2002) *J. Vac. Sci. Technol., A*, **20**, 802–808.
54 Musschoot, J., Deduytsche, D., Poelman, H., Haemers, J., Van Meirhaeghe, R.L., Van den Berghe, S., and Detavernier, C. (2009) *J. Electrochem. Soc.*, **156**, P122–P126.
55 Sauerbrey, G. (1959) *Z. Angew. Phys.*, **155**, 206–222.
56 Ballantine, D.S. (1997) *Acoustic Wave Sensors*, Academic Press.
57 Elam, J.W., Groner, M.D., and George, S.M. (2002) *Rev. Sci. Instrum.*, **73**, 2981.
58 Rocklein, M.N. and George, S.M. (2003) *Anal. Chem.*, **75**, 4975–4982.
59 Paul, W. and Steinwedel, H. (1953) *Z. Naturforsch.*, **80**, 448.
60 Dawson, P. (1976) *Quadrupole Mass Spectrometry*, Elsevier, Amsterdam.
61 Ritala, M., Juppo, M., Kukli, K., Rahtu, A., and Leskelä, M. (1999) *J. Phys. IV*, **9**, 8.
62 Juppo, M., Rahtu, A., Ritala, M., and Leskelä, M. (2000) *Langmuir*, **16**, 4034–4039.
63 Henn-Lecordier, L., Lei, W., Anderle, M., and Rubloff, G.W. (2007) *J. Vac. Sci. Technol., B*, **25**, 130–139.
64 Fujiware, H. (2007) *Spectroscopic Ellipsometry – Principles and Applications*, Wiley.
65 Langereis, E., Heil, S.B.S., Knoops, H.C.M., Keuning, W., van de Sanden, M.C.M., and Kessels, W.M.M. (2009) *J. Phys. D: Appl. Phys.*, **42**, 073001.
66 Chabal, Y.J. (1988) *Surf. Sci. Rep.*, **8**, 211–357.
67 Dillon, A.C., Ott, A.W., Way, J.D., and George, S.M. (1995) *Surf. Sci.*, **322**, 230.
68 Kwon, J., Dai, M., Halls, M.D., Langereis, E., Chabal, Y.J., and Gordon, R.G. (2009) *J. Phys. Chem. C*, **113**, 654.
69 Goldstein, D.N., Mccormick, J.A., and George, S.M. (2008) *J. Phys. Chem.*, **112**, 19530–19539.
70 Rai, V.R. and Agarwal, S. (2012) *J. Vac. Sci. Technol., A*, **30**, 01A158.
71 Sperling, B., Kimes, W., and Maslar, J.E. (2010) *Appl. Surf. Sci.*, **256**, 5035–5041.

72 Mackus, A.J.M., Heil, S.B.S., Langereis, E., Knoops, H.C.M., van de Sanden, M.C.M., and Kessels, W.M.M. (2010) *J. Vac. Sci. Technol., A*, **28**, 77–87.
73 Bankras, R., Holleman, J., Schmitz, J., Sturm, M., Zinine, A., Wormeester, H., and Poelsema, B. (2006) *Chem. Vap. Deposition*, **12**, 275–279.
74 Nilsen, O. and Fjellvåg, H. (2011) *J. Therm. Anal. Calorim.*, **105**, 33–37.
75 Schuisky, M., Elam, J.W., and George, S.M. (2002) *Appl. Phys. Lett.*, **81**, 180–182.
76 Koukitu, A., Kumagai, T., Taki, T., and Seki, H. (1999) *Jpn. J. Appl. Phys.*, **38**, 4980–4982.
77 Rosental, A., Adamson, P., Gerst, A., and Niilisk, A. (1996) *Appl. Surf. Sci.*, **107**, 178–183.
78 Berland, B.S., Gartland, I.P., Ott, A.W., and George, S.M. (1998) *Chem. Mater.*, **10**, 3941–3950.
79 Dendooven, J., Devloo-Casier, K., Levrau, E., Van Hove, R., Sree, S.P., Baklanov, M.R., Martens, J.A., and Detavernier, C. (2012) *Langmuir*, **28**, 3852.
80 Devloo-Casier, K., Ludwig, K.F., Detavernier, C., and Dendooven, J. (2014) *J. Vac. Sci. Technol., A*, **32**, 010801.
81 Dendooven, J., Pulinthanathu Sree, S., De Keyser, K., Deduytsche, D., Martens, J.A., Ludwig, K.F., and Detavernier, C. (2011) *J. Phys. Chem. C*, **115**, 6605.
82 Fong, D.D., Eastman, J.A., Kim, S.K., Fister, T.T., Highland, M.J., Baldo, P.M., and Fuoss, P.H. (2010) *Appl. Phys. Lett.*, **97**, 191904.
83 Setthapun, W., Williams, W.D., Kim, S.M., Feng, H., Elam, J.W., Rabuffetti, F.A., Poeppelmeier, K.R., Stair, P.C., Stach, E.A., Ribeiro, F.H., Miller, J.T., and Marshall, C.L. (2010) *J. Phys. Chem. C*, **114**, 9758–9771.
84 Filez, M., Poelman, H., Ramachandran, R.K., Dendooven, J., Devloo-Casier, K., Fonda, E., Detavernier, C., and Marin, G.B. (2014) *Catal. Today*, **229**, 2–13.
85 Devloo-Casier, K., Dendooven, J., Ludwig, K.F., Lekens, G., D'Haen, J., and Detavernier, C. (2011) *Appl. Phys. Lett.*, **98**, 231905.
86 Dendooven, J., Devloo-Casier, K., Ide, M., Grandfield, K., Kurttepeli, M., Ludwig, K.F., Bals, S., Van Der Voort, P., and Detaverniera, C. (2014) *Nanoscale*, **6**, 14991–14998.
87 Dücsö, C., Khanh, N.Q., Horvath, Z., Barsony, I., Utriainen, M., Lehto, S., Nieminen, M., and Niinistö, L. (1996) *J. Electrochem. Soc.*, **143**, 683–687.
88 Ott, A.W., Klaus, J.W., Johnson, J.M., George, S.M., McCarley, K.C., and Way, J.D. (1997) *Chem. Mater.*, **9**, 707–714.
89 Ritala, M., Leskelä, M., Dekker, J.-P., Mutsaers, C., Soininen, P.J., and Skarp, J. (1999) *Chem. Vap. Deposition*, **5**, 7–9.
90 Hämäläinen, J., Munnik, F., Ritala, M., and Leskelä, M. (2008) *Chem. Mater.*, **20**, 6840–6846.
91 Diskus, M., Nilsen, O., and Fjellvåg, H. (2011) *Chem. Vap. Deposition*, **17**, 135–140.
92 Masuda, H. and Satoh, M. (1996) *Jpn. J. Appl. Phys., Part 2*, **35**, L126–L129.
93 Thompson, G.E. (1997) *Thin Solid Films*, **297**, 192–201.

94 Jessensky, O., Muller, F., and Gösele, U. (1998) *Appl. Phys. Lett.*, **72**, 1173–1175.
95 Elam, J.W., Libera, J.A., Pellin, M.J., and Stair, P.C. (2007) *Appl. Phys. Lett.*, **91**, 243105.
96 Becker, J.S., Suh, S., Wang, S.L., and Gordon, R.G. (2003) *Chem. Mater.*, **15**, 2969–2976.
97 Dendooven, J., Deduytsche, D., Musschoot, J., Vanmeirhaeghe, R.L., and Detavernier, C. (2009) *J. Electrochem. Soc.*, **156**, P63–P67.
98 Dendooven, J., Deduytsche, D., Musschoot, J., Vanmeirhaeghe, R.L., and Detavernier, C. (2010) *J. Electrochem. Soc.*, **157**, G111–G116.
99 Musschoot, J., Dendooven, J., Deduytsche, D., Haemers, J., Buyle, G., and Detavernier, C. (2012) *Surf. Coat. Technol.*, **206**, 4511–4517.
100 Gao, F., Arpiainen, S., and Puurunen, R.L. (2015) *J. Vac. Sci. Technol., A*, **33**, 010601.
101 Gordon, R.G., Hausmann, D., Kim, E., and Shepard, J. (2003) *Chem. Vap. Deposition*, **9**, 73–78.
102 Gordon, R. G. (2008) *Step Coverage by ALD Films: Theory and Examples of Ideal and Non-ideal Reactions*. Presented at the AVS Topical Conference on ALD, Bruges, Belgium, June 29–July 2.
103 Knudsen, M. (1909) *Ann. Phys.*, **333**, 75–130.
104 In, S.R. (1998) *J. Vac. Sci. Technol., A*, **16**, 3495–3501.
105 Dendooven, J., Musschoot, J., Deduytsche, D., Vanmeirhaeghe, R., and Detavernier, C. (2008) *Conformality of Thermal and Plasma Enhanced ALD*. Presented at the AVS Topical Conference on ALD, Bruges, Belgium, June 29–July 2.
106 Knoops, H.C.M., Langereis, E., van de Sanden, M.C.M., and Kessels, W.M.M. (2010) *J. Electrochem. Soc.*, **157**, G241–G249.
107 Macko, P., Veis, P., and Cernogora, G. (2004) *Plasma Sources Sci. Technol.*, **13**, 251–262.
108 Adams, S.F. and Miller, T.A. (2000) *Plasma Sources Sci. Technol.*, **9**, 248–255.
109 Cvelbar, U., Mozetic, M., and Ricard, A. (2005) *IEEE Trans. Plasma Sci.*, **33**, 834–837.
110 Tserepi, A.D. and Miller, T.A. (1994) *J. Appl. Phys.*, **75**, 7231–7236.
111 Gomez, S., Steen, P.G., and Graham, W.G. (2002) *Appl. Phys. Lett.*, **81**, 19–21.
112 Kim, Y.C. and Boudart, M. (1991) *Langmuir*, **7**, 2999–3005.
113 Cartry, G., Duten, X., and Rousseau, A. (2006) *Plasma Sources Sci. Technol.*, **15**, 479–488.
114 Guyon, C., Cavadias, S., Mabille, I., Moscosa-Santillan, M., and Amouroux, J. (2004) *Catal. Today*, **89**, 159–167.
115 Wood, B.J. and Wise, H. (1961) *J. Phys. Chem.*, **65**, 1976.
116 van Hemmen, J.L., Heil, S.B.S., Klootwijk, J.H., Roozeboom, F., Hodson, C.J., van de Sanden, M.C.M., and Kessels, W.M.M. (2007) *J. Electrochem. Soc.*, **154**, G165–G169.
117 Dingemans, G., van Helvoirt, C.A.A., Pierreux, D., Keuning, W., and Kessels, W.M.M. (2012) *J. Electrochem. Soc.*, **159**, H277–H285.

118 Kubala, N.G., Rowlette, P.C., and Wolden, C.A. (2009) *J. Phys. Chem. C*, **113**, 16307–16310.

119 van den Oever, P.J., van Helden, J.H., Lamers, C.C.H., Engeln, R., Schram, D.C., van de Sanden, M.C.M., and Kessels, W.M.M. (2005) *J. Appl. Phys.*, **98**, 093301.

120 Shin, H.J., Jeong, D.K., Lee, J.G., Sung, M.M., and Kim, J.Y. (2004) *Adv. Mater.*, **16**, 1197.

121 Daub, M., Knez, M., Gösele, U., and Nielsch, K. (2007) *J. Appl. Phys.*, **101**, 09J111.

122 Gu, D., Baumgart, H., Abdel-Fattah, T.M., and Namkoong, G. (2010) *ACS Nano*, **4**, 753–758.

123 Sander, M.S., Cote, M.J., Gu, W., Kile, B.M., and Tripp, C.P. (2004) *Adv. Mater.*, **16**, 2052.

124 Yang, C.-J., Wang, S.-M., Liang, S.-W., Chang, Y.-H., Chen, C., and Shieh, J.-M. (2007) *Appl. Phys. Lett.*, **90**, 033104.

125 Kim, W.-H., Park, S.-J., Son, J.-Y., and Kim, H. (2008) *Nanotechnology*, **19**, 045302.

126 Chong, Y.T., Goerlitz, D., Martens, S., Yau, M.Y.E., Allende, S., Bachmann, J., and Nielsch, K. (2010) *Adv. Mater.*, **22**, 2435.

127 Bae, C., Yoon, Y., Yoo, H., Han, D., Cho, J., Lee, B.H., Sung, M.M., Lee, M., Kim, J., and Shin, H. (2009) *Chem. Mater.*, **21**, 2574–2576.

128 Kemell, M., Pore, V., Tupala, J., Ritala, M., and Leskelä, M. (2007) *Chem. Mater.*, **19**, 1816–1820.

129 Ng, C.J.W., Gao, H., and Tan, T.T.Y. (2008) *Nanotechnology*, **19**, 445604.

130 Liang, Y.-C., Wang, C.-C., Kei, C.-C., Hsueh, Y.-C., Cho, W.-H., and Perng, T.-P. (2011) *J. Phys. Chem. C*, **115**, 9498–9502.

131 Rugge, A., Becker, J.S., Gordon, R.G., and Tolbert, S.H. (2003) *Nano Lett.*, **3**, 1293–1297.

132 King, J.S., Graugnard, E., and Summers, C.J. (2005) *Adv. Mater.*, **17**, 1010.

133 King, J.S., Heineman, D., Graugnard, E., and Summers, C.J. (2005) *Appl. Surf. Sci.*, **244**, 511–516.

134 Graugnard, E., Chawla, V., Lorang, D., and Summers, C.J. (2006) *Appl. Phys. Lett.*, **89**, 211102.

135 Sechrist, Z.A., Schwartz, B.T., Lee, J.H., McCormick, J.A., Piestun, R., Park, W., and George, S.M. (2006) *Chem. Mater.*, **18**, 3562–3570.

136 Povey, I.M., Bardosova, M., Chalvet, F., Pemble, M.E., and Yates, H.M. (2007) *Surf. Coat. Technol.*, **201**, 9345–9348.

137 Hwang, D.-K., Noh, H., Cao, H., and Chang, R.P.H. (2009) *Appl. Phys. Lett.*, **95**, 091101.

138 Karuturi, S.K., Liu, L., Su, L.T., Zhao, Y., Fan, H.J., Ge, X., He, S., and Yoong, A.T.I. (2010) *J. Phys. Chem. C*, **114**, 14843–14848.

139 Cameron, M.A., Gartland, I.P., Smith, J.A., Diaz, S.F., and George, S.M. (2000) *Langmuir*, **16**, 7435–7444.

140 Pan, M., Cooper, C., Lin, Y., and Meng, G. (1999) *J. Membr. Sci.*, **158**, 235–241.

141 Cooper, C.A. and Lin, Y.S. (2002) *J. Membr. Sci.*, **195**, 35–50.

142 McCool, B.A. and DeSisto, W.J. (2004) *Chem. Vap. Deposition*, **10**, 190.

143 McCool, B.A. and DeSisto, W.J. (2004) *Ind. Eng. Chem. Res.*, **43**, 2478–2484.

144 Schuring, D. (2002) Diffusion in zeolites: Towards a microscopic understanding, PhD thesis. Eindhoven University of Technology.

145 Velleman, L., Triani, G., Evans, P.J., Shapter, J.G., and Losic, D. (2009) *Microporous Mesoporous Mater.*, **126**, 87–94.

146 Chen, Z., Jiang, Y., Dunphy, D.R., Adams, D.P., Hodges, C., Liu, N., Zhang, N., Xomeritakis, G., Jin, X., Aluru, N.R., Gaik, S.J., Hillhouse, H.W., and Brinker, C.J. (2010) *Nat. Mater.*, **9**, 667–675.

147 Dendooven, J., Pulinthanathu Sree, S., De Keyser, K., Deduytsche, D., Martens, J.A., Ludwig, K.F., and Detavernier, C. (2011) *J. Phys. Chem. C*, **115**, 6605–6610.

148 Davie, M.E., Foerster, T., Parsons, S., Pulham, C., Rankin, D.W.H., and Smart, B.A. (2006) *Polyhedron*, **25**, 923–929.

149 Dendooven, J., Goris, B., Devloo-Casier, K., Levrau, E., Biermans, E., Baklanov, M.R., Ludwig, K.F., Van Der Voort, P., Bals, S., and Detavernier, C. (2012) *Chem. Mater.*, **24**, 1992–1994.